AGU PUBLICATIONS

JGR

Journal of Geophysical Research: Oceans

RESEARCH ARTICLE

10.1002/2017JC013191

Characterization of Particle Backscattering of Global Highly Turbid Waters From VIIRS Ocean Color Observations

Wei Shi[1,2] and Menghua Wang[1]

[1]NOAA National Environmental Satellite, Data, and Information Service, Center for Satellite Applications and Research, College Park, MD, USA, [2]CIRA at Colorado State University, Fort Collins, CO, USA

Key Points:
- A NIR-based $b_{bp}(\lambda)$ algorithm for turbid coastal and inland waters has been developed and used in this study
- Seasonal and interannual variations of $b_{bp}(\lambda)$ in the world most turbid waters are characterized and quantified
- A new combined NIR-based and Quasi-Analytical Algorithm (QAA)-based $b_{bp}(\lambda)$ algorithm is proposed and demonstrated to improve global $b_{bp}(\lambda)$

Correspondence to:
W. Shi,
wei.1.shi@noaa.gov

Citation:
Shi, W., & Wang, M. (2017). Characterization of particle backscattering of global highly turbid waters from VIIRS ocean color observations. *Journal of Geophysical Research: Oceans*, *122*, 9255–9275. https://doi.org/10.1002/2017JC013191

Received 13 JUN 2017
Accepted 7 OCT 2017
Accepted article online 13 OCT 2017
Published online 30 NOV 2017

Abstract Normalized water-leaving radiance spectra $nL_w(\lambda)$ at the near-infrared (NIR) from five years of observations (2012–2016) with the Visible Infrared Imaging Radiometer Suite (VIIRS) onboard the Suomi National Polar-orbiting Partnership (SNPP) are used to derive the particle backscattering coefficients $b_{bp}(\lambda)$ for global highly turbid coastal and inland waters. Based on the fact that the absorption coefficient of sea water $a_w(\lambda)$ is generally much larger than those of the other constituents $a_{iop}(\lambda)$ at the NIR wavelengths in coastal and inland waters, an NIR-based $b_{bp}(\lambda)$ algorithm for turbid coastal and inland waters has been developed and used in this study. This algorithm can be safely used for highly turbid waters with $nL_w(745)$ and $nL_w(862) < \sim 6$ and ~ 4 mW cm^{-2} μm^{-1} sr^{-1}, respectively. Seasonal and interannual variations of $b_{bp}(\lambda)$ in China's east coastal region, the Amazon River Estuary, the La Plata River Estuary, the Meghna River Estuary, the Atchafalaya River Estuary, and Lake Taihu are characterized and quantified. The coefficient $b_{bp}(\lambda)$ can reach over $\sim$3–4 m^{-1} in the Amazon River Estuary and China's east coastal region. The Amazon River Estuary is identified as the most turbid region in the global ocean in terms of $b_{bp}(\lambda)$ magnitude. $b_{bp}(\lambda)$ spectra in these five highly turbid regions are also seasonal-dependent and regional-dependent. In the highly turbid waters of China's east coastal region and the Amazon River Estuary, $b_{bp}(\lambda)$ generally increases in wavelength from 410 to 862 nm, while it decreases in the La Plata River Estuary and Atchafalaya River Estuary. This is attributed to the different particle size distributions in these waters. The geophysical implication of the $b_{bp}(\lambda)$ spectral curvatures for different waters is discussed. To improve global $b_{bp}(\lambda)$ for both open oceans and coastal turbid waters, a new combined NIR-based and Quasi-Analytical Algorithm (QAA)-based $b_{bp}(\lambda)$ algorithm is proposed and demonstrated.

1. Introduction

Normalized water-leaving radiance spectra $nL_w(\lambda)$ derived from satellite observations such as the Moderate Resolution Imaging Spectroradiometer (MODIS) (Esaias et al., 1998) and the Visible Infrared Imaging Radiometer Suite (VIIRS) on the Suomi National Polar-orbiting Partnership (SNPP) (Goldberg et al., 2013) are intrinsically related to the inherent optical properties (IOPs) of the constituents of the sea water (Garver & Siegel, 1997; Gordon et al., 1988; Lee et al., 2002; Werdell et al., 2013). As one of the most important IOPs, the particle backscattering coefficient ($b_{bp}(\lambda)$) is determined by the optical features of the particles such as the refractive index of the particles, particle backscattering ratio, and particle size distribution in the sea water (Babin et al., 2003; Kostadinov et al., 2009; Stramski et al., 2007; Ulloa et al., 1994). In the coastal region, the backscattering of suspended phytoplankton particles and mineral particles is generally one of the most important determinants of the normalized water-leaving radiance spectra as observed from satellite ocean color measurements.

Since the launch of the Coast Zone Color Scanner (CZCS) in 1978 (Gordon et al., 1980; Hovis et al., 1980), satellite ocean color remote sensing has been primarily focusing on visible wavelengths (ocean color). High-quality ocean color products with uncertainties for $nL_w(\lambda)$ at the blue within $\sim$5% and chlorophyll-a (Chl-a) within $\sim$35% have been produced in global open oceans (McClain, 2009; McClain et al., 2004). These satellite ocean color products derived from visible wavelengths have been helping us to study and understand the global and regional ocean optical, biological, and ecological processes and phenomena, as well as help to monitor for natural hazards. However, in coastal regions, especially in highly turbid coastal regions such as river estuaries and inland waters, there are still some challenges in deriving accurate $nL_w(\lambda)$ spectra in

wavelengths between blue and near-infrared (NIR), and ocean biological and biogeochemical products such Chl-a concentration (O'Reilly et al., 1998), the water diffuse attenuation coefficient at the wavelength of 490 nm $K_d(490)$ (Wang et al., 2009a), and the ocean's inherent optical properties (IOPs) (Lee et al., 2002; Werdell et al., 2013). These challenges largely root from two causes in producing satellite ocean color products in the coastal turbid waters, i.e., errors in atmospheric correction and unsuitable algorithms for ocean biological and biogeochemical product retrievals.

The ocean is generally black at the NIR (certainly at the shortwave infrared (SWIR)) wavelengths for the open ocean. Thus, ocean color products from satellite sensors such as MODIS on the Aqua satellite have been routinely derived using the two MODIS NIR bands (748 and 869 nm) (Gordon & Wang, 1994) with the assumption of a black ocean in the NIR for the open ocean. For turbid coastal and inland waters, however, the NIR black ocean assumption is often invalid (Lavender et al., 2005; Ruddick et al., 2000; Siegel et al., 2000; Wang & Shi, 2005). Even though some modifications were implemented to account for the NIR ocean contributions for productive (but not very turbid) near-shore or coastal waters (Bailey et al., 2010; Jiang & Wang, 2014; Ruddick et al., 2000; Siegel et al., 2000; Wang et al., 2012), satellite-derived $nL_w(\lambda)$ spectra in highly turbid waters can still be in error (Jiang & Wang, 2014; Shi & Wang, 2014). Wang et al. (2012) show that satellite-derived $nL_w(\lambda)$ spectra using the NIR atmospheric correction can be significantly biased low, and can even become negative in the blue bands in the highly turbid Yellow Sea region. On the other hand, the majority of the algorithms such as Chl-a (O'Reilly et al., 1998) and IOP algorithms (Garver & Siegel, 1997; Lee et al., 2002; Werdell et al., 2013) are derived and optimized for global open oceans and not for turbid coastal and inland waters. The different water properties and highly dynamic features of the complex coastal waters (especially highly turbid waters) can lead to poor accuracy of the ocean color products in coastal turbid regions.

It was demonstrated that the ocean black pixel assumption of the SWIR bands for MODIS is generally valid for the world's most turbid waters (Shi & Wang, 2009b; Wang & Shi, 2005). Thus, satellite measurements at two MODIS or VIIRS SWIR bands can be used to derive $nL_w(\lambda)$ spectra from visible to the NIR and SWIR 1,240 nm band (Wang, 2007). In fact, MODIS-Aqua measurements at the SWIR bands were used to carry out atmospheric correction in order to study the physical, optical, biological, and biogeochemical processes in the Bohai Sea (BS), Yellow Sea (YS), and East China Sea (ECS) (Shi et al., 2011; Shi & Wang, 2012a, 2012b, 2012c), as well as in the inland Lake Taihu (Wang et al., 2011, 2013a).

Unlike the open ocean waters, the $nL_w(\lambda)$ spectral feature in the coastal turbid region is significantly enhanced in the spectral range of red and NIR bands (Shi & Wang, 2014). Thus, accurate retrievals of the $nL_w(\lambda)$ spectra in red and NIR bands from the SWIR atmospheric correction algorithm provide further optical information about the ocean (water) beyond traditional blue and green wavelengths to address the complexity of coastal and inland turbid waters. Indeed, satellite and in situ $nL_w(\lambda)$ data in red and NIR wavelengths have been used to characterize and quantify water properties in coastal and inland waters such as Chl-a concentration (Gitelson et al., 2007), floating green algae blooms (Hu et al., 2010; Shi & Wang, 2009c), river plumes (Nezlin et al., 2008; Shi & Wang, 2009a), total suspended matter (TSM) (Miller & McKee, 2004; Shen et al., 2010a; Son & Wang, 2012; Zhang et al., 2010b), the light diffuse attenuation coefficient at 490 nm (Wang et al., 2009a; Zhang et al., 2012), and ocean optical and biological property variations in the Korean dump site in the Yellow Sea (Son et al., 2011).

Using the diffuse attenuation coefficient at the wavelength of 490 nm, $K_d(490)$, which was derived from measurements of MODIS-Aqua, Shi and Wang (2010b) characterized global ocean turbidity. Turbid waters with $K_d(490)$ over $\sim$0.3 m^{-1} are all located in coastal regions, river estuaries, and inland lakes with an average global coverage of $\sim$0.74%, accounting for $\sim$8–12% of the total global continental shelf area. The Amazon River Estuary ranks as the world's most turbid region with the mean $K_d(490)$ value of over $\sim$5 m^{-1}. Major highly turbid waters also include China's east coastal region, La Plata River Estuary in the Southern Hemisphere, and Meghna River in the Bay of Bengal. Coastal regions along the US East Coast and the Gulf of Mexico coast such as the Chesapeake Bay and Mississippi River Estuary are also highly turbid with $K_d(490)$ generally over $\sim$1 m^{-1}.

The IOPs are the absorption and scattering of the constituents in the water column, i.e., pure water, phytoplankton, color dissolved organic matter (CDOM), and minerals. The spectrum and radiance distribution of the light emerging from the ocean and derived from satellite ocean color observations are determined by

the IOP properties. Numerous studies were conducted to retrieve these IOP parameters from satellite ocean color observations (Garver & Siegel, 1997; Hoge & Lyon, 1996; Lee et al., 2002; Werdell et al., 2013). However, most of these studies are focused on open ocean and less turbid waters. In fact, only $nL_w(\lambda)$ spectra in the visible are used in these IOP retrieval algorithms. Improvements were also made to tune these algorithms with the in situ $nL_w(\lambda)$ spectra in the NIR wavelengths in some regional studies (Huang et al., 2014; Le et al., 2009; Qing et al., 2011).

In this study, we use $nL_w(\lambda)$ at the VIIRS NIR bands of 745 and 862 nm derived from the SWIR atmospheric correction algorithm with VIIRS-SNPP observations between 2012 and 2016 to compute the $b_{bp}(\lambda)$ in the VIIRS visible and NIR bands for the major highly turbid regions of the global ocean. Spatial and temporal variations of the $b_{bp}(\lambda)$ are characterized and quantified in these regions. The advantages of this NIR-based $b_{bp}(\lambda)$ algorithm for the turbid waters and implications of $b_{bp}(\lambda)$ spectra are discussed. The $b_{bp}(\lambda)$ data from the NIR-based $b_{bp}(\lambda)$ retrieval algorithm are also compared with those from the Quasi-Analytical Algorithm (QAA) (Lee et al., 2002) over the highly turbid regions. A scheme is proposed to combine these two $b_{bp}(\lambda)$ algorithms when producing global $b_{bp}(\lambda)$ products from VIIRS-SNPP observations for both clear open ocean and turbid coastal/inland waters.

2. Methods and Data

2.1. VIIRS-SNPP Data and the SWIR Ocean Color Data Processing

VIIRS is one of the key instruments onboard the SNPP satellite launched on 28 October 2011. VIIRS has 22 spectral bands covering a spectral range of 0.410–12.013 μm, which includes 14 reflective solar bands (RSBs), 7 thermal emissive bands (TEBs), and a panchromatic day/night band (DNB). VIIRS has similar spectral bands to MODIS, providing observations of Earth's atmosphere, land, and ocean properties (Goldberg et al., 2013). One of the primary goals of the VIIRS mission is to provide data continuity from MODIS for the science and user communities with the Environmental Data Records (EDR) (or Level-2 data) over global oceanic waters to enable assessment of climatic and environmental variability (McClain, 2009). Additionally, ocean color EDR is a key product suite derived from VIIRS (Wang et al., 2013b, 2016a).

Specifically, VIIRS-SNPP has five visible bands (M1–M5) with nominal central wavelengths of 410, 443, 486, 551, and 671 nm, two NIR bands (M6 and M7) at wavelengths of 745 and 862 nm, and three SWIR bands (M8, M10, and M11) at wavelengths of 1,238, 1,601, and 2,257 nm for satellite ocean color data processing. These spectral bands are at a moderate spatial resolution of 750 m. On-orbit vicarious calibrations for VIIRS-SNPP were carefully carried out using the in situ $nL_w(\lambda)$ spectra from the Marine Optical Buoy (MOBY) (Clark et al., 1997) in the waters off Hawaii and over the South Pacific Gyre (SPG) (Wang et al., 2016b). Similar to the standard NIR atmospheric correction algorithm (Gordon & Wang, 1994; IOCCG, 2010) with the two NIR bands (745 and 862 nm for VIIRS), the SWIR-based atmospheric correction algorithm (Wang, 2007) with VIIRS SWIR bands at 1,238 and 1,601 nm has been used (Wang et al., 2013b) in deriving $nL_w(\lambda)$ spectra in this study.

The Multi-Sensor Level-1 to Level-2 (MSL12), which is the official NOAA VIIRS ocean color data processing system, has been used for processing satellite ocean color data from Sensor Data Records (SDR) (or Level-1B data) to ocean color EDR (or Level-2 data) products for VIIRS-SNPP (Wang et al., 2013b, 2016a). MSL12 was developed for the purpose of using a consistent and common data processing system to produce ocean color data from multiple satellite ocean color sensors (Wang, 1999; Wang et al., 2002; Wang & Franz, 2000). In recent years, MSL12 has made several important improvements and enhancements. In particular, these improvements and updates include the SWIR-based and NIR-SWIR combined atmospheric correction algorithms for improved ocean color data products in coastal and inland waters (Wang, 2007; Wang et al., 2009b; Wang & Shi, 2007). In this study, VIIRS-SNPP observations over the highly turbid regions in China's east coast, the Amazon River Estuary, the La Plata River Estuary between Uruguay and Argentina, the Meghna River Estuary in the Bay of Bengal, the Atchafalaya River Estuary in distributaries of the Mississippi River, and the inland fresh water Lake Taihu between 2012 and 2016 were processed using the MSL12 ocean color data processing system (SWIR-based) to produce $nL_w(\lambda)$ at visible and NIR bands in order to derive $b_{bp}(\lambda)$ in these regions.

2.2. The NIR-Based $b_{bp}(\lambda)$ Algorithm for VIIRS-SNPP Observations

Satellite-measured $nL_w(\lambda)$ data are intrinsically related to the water constituents such as CDOM, phytoplankton particles, inorganic sediments, etc. (Gordon et al., 1988). The specific spectral features of each

constituent such as absorption coefficient $a(\lambda)$ and particle backscattering coefficient $b_{bp}(\lambda)$ determine the spectral variability of $nL_w(\lambda)$ spectra or remote sensing reflectance just beneath the surface $r_{rs}(\lambda)$, i.e.,

$$r_{rs}(\lambda)=\frac{R_{rs}(\lambda)}{0.52+1.7R_{rs}(\lambda)}, \tag{1}$$

where $R_{rs}(\lambda)$ is the remote sensing reflectance above the surface, which can be directly computed from $nL_w(\lambda)$, i.e., $R_{rs}(\lambda) = nL_w(\lambda)/F_0(\lambda)$ with $F_0(\lambda)$ the extraterrestrial solar irradiance.

Gordon et al. (1988) developed a quadratic model between $r_{rs}(\lambda)$ and ocean's IOPs, i.e.,

$$r_{rs}(\lambda)=g_1\left(\frac{b_b(\lambda)}{a(\lambda)+b_b(\lambda)}\right)+g_2\left(\frac{b_b(\lambda)}{a(\lambda)+b_b(\lambda)}\right)^2, \tag{2}$$

where g_1 and g_2 are the constant values of 0.0949 and 0.0794 as derived in Gordon et al. (1994). Coefficients $a(\lambda)$ and $b_b(\lambda)$ are total absorption and backscattering coefficients, respectively, which can be expressed as

$$a(\lambda)=a_w(\lambda)+a_{ph}(\lambda)+a_g(\lambda)+a_d(\lambda), \tag{3}$$

$$b_b(\lambda)=b_{bw}(\lambda)+b_{bp}(\lambda), \tag{4}$$

where $a_w(\lambda)$, $a_{ph}(\lambda)$, $a_g(\lambda)$, and $a_d(\lambda)$ are the absorption coefficients for pure seawater, phytoplankton, dissolved matter, and nonalgal particles, respectively, and $b_{bw}(\lambda)$ and $b_{bp}(\lambda)$ are the backscattering coefficients for pure seawater and particulate matters, respectively. In a recent study, Shi and Wang (2014) demonstrated an NIR-based IOP algorithm to retrieve the $b_{bp}(\lambda)$ in the coastal turbid waters based on the spectral features of the absorptions of pure seawater $a_w(\lambda)$, phytoplankton $a_{ph}(\lambda)$, dissolved matters $a_g(\lambda)$, and nonalgal particles absorption $a_d(\lambda)$ at the NIR wavelengths. Briefly, pure seawater absorption coefficients $a_w(\lambda)$ at the NIR bands are typically significantly higher than those from other constituents, i.e., $a_w(\lambda) \gg a_{ph}(\lambda)$, $a_g(\lambda)$, and $a_d(\lambda)$. For example, $a_w(869)$ is $\sim$5 m^{-1} as compared to $a_{ph}(\lambda)$, $a_g(\lambda)$, and $a_d(\lambda)$ at 869 nm that are normally negligible in comparison with $a_w(869)$. Therefore, with the spectral features of $a_w(\lambda)$, $a_{ph}(\lambda)$, $a_g(\lambda)$, and $a_d(\lambda)$ at the VIIRS 745 and 862 nm bands, $b_b(\lambda)/(a(\lambda)+b_b(\lambda))$ can be approximated as

$$\left(\frac{b_b(\lambda)}{a(\lambda)+b_b(\lambda)}\right)\approx\left(\frac{b_b(\lambda)}{a_w(\lambda)+b_b(\lambda)}\right). \tag{5}$$

It is noted that $b_b(\lambda)/(a(\lambda)+b_b(\lambda))$ is approximated to be $\sim$1.0 in the extremely turbid waters when $b_b(\lambda) \gg a_w(\lambda)$, and consequently $nL_w(745)$ and $nL_w(862)$ become less sensitive to the change of $b_{bp}(\lambda)$ (or TSM concentration). This indicates that any small error of satellite-derived $nL_w(745)$ and $nL_w(862)$ can lead to significant bias in the VIIRS-derived $b_{bp}(\lambda)$. In situ measurements (Knaeps et al., 2015; Shen et al., 2010a, 2010b) indeed show that $nL_w(\lambda)$ at the NIR wavelengths become saturated when TSM concentrations are over $\sim$1000 mg/L. Shi and Wang (2009b) also show that MODIS-derived $nL_w(748)$ and $nL_w(859)$ can become less sensitive to the $nL_w(1{,}240)$ at the SWIR wavelength which is a surrogate for TSM concentrations in extremely turbid waters when $nL_w(748)$ and $nL_w(859)$ are over $\sim$6 and $\sim$4 mW cm^{-2} μm^{-1} sr^{-1}, respectively. These results are consistent with in situ observations (Knaeps et al., 2015; Shen et al., 2010a, 2010b).

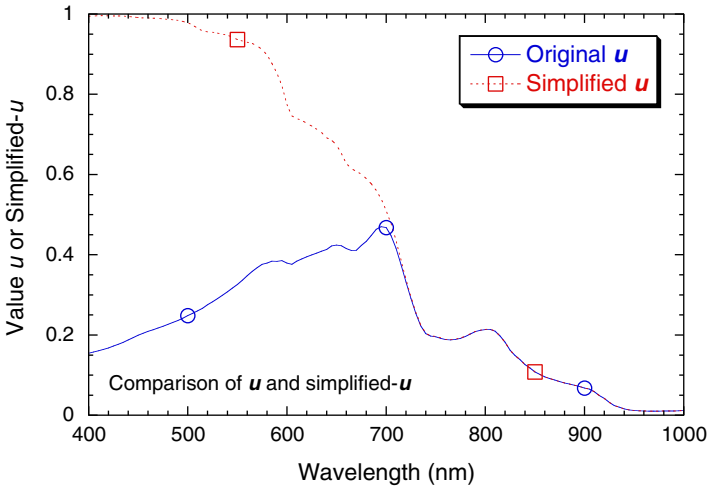

Figure 1. Comparison of $b_b(\lambda)/(a(\lambda)+b_b(\lambda))$ ($u(\lambda)$, dash line) and $b_b(\lambda)/(a_w(\lambda)+b_b(\lambda))$ (simplified-$u(\lambda)$, solid line) for a typical coastal turbid water. TSM is assumed to be 50 mg/L, Chl-a concentration is set to be constant at 20 mg/m^3, the CDOM absorption at 440 nm $a_g(440)$ is 1.0 m^{-1}.

For VIIRS observations, equation (5) can be safely used to derive $b_{bp}(\lambda)$ when VIIRS $nL_w(745)$ and $nL_w(862)$ are $<\sim$6 and $\sim$4 mW cm^{-2} μm^{-1} sr^{-1}, respectively. For extremely turbid waters with $nL_w(745)$ and $nL_w(862) > \sim$6 and $\sim$4 mW cm^{-2} μm^{-1} sr^{-1}, however, cautions should be given and biased $b_{bp}(\lambda)$ retrievals may be possible when applying this approach to derive $b_{bp}(\lambda)$.

Figure 1 is an example to show the comparison of $b_b(\lambda)/(a(\lambda)+b_b(\lambda))$ (represented as $u(\lambda)$) and $b_b(\lambda)/(a_w(\lambda)+b_b(\lambda))$ (represented as simplified-$u(\lambda)$) in the wavelengths between 400 and 1,000 nm. The IOP data for this example is selected from the Hydrolight 5.3 software

package (Mobley et al., 1993) for typical coastal turbid Case-2 water. The Chl-a concentration is set as a constant at 20 mg/m^3, CDOM absorption at 440 nm $a_g(440)$ is 1.0 m^{-1}, and the mineral concentration is 50 mg/L with the specific absorption and scattering set as the average of calcareous sand, red clay, yellow clay, and brown earth, which are typical sediment mineral types in the coastal regions.

In Figure 1, $u(\lambda)$ and simplified-$u(\lambda)$ are significantly different in visible wavelengths between 400 and 700 nm. Specifically, $u(\lambda)$ and simplified-$u(\lambda)$ are 0.155 and 0.994 at the wavelength of 400 nm, respectively. However, $b_{bp}(400)$ is about over two orders higher than $a_w(400)$. This leads simplified-$u(400)$ to be close to 1.0. On the other hand, $a(400)$ is also significantly higher than $a_w(400)$, and in the same order as the $b_{bp}(400)$, thus $u(400)$ is lower than simplified-$u(400)$. However, $u(\lambda)$ and simplified-$u(\lambda)$ become very close at the NIR bands due to a significant increase of $a_w(\lambda)$ as shown in Figure 1. At the two NIR bands of 745 and 862 nm, $u(745)$ and $u(862)$ are 0.1974 and 0.0956, respectively, while simplified-$u(745)$ and simplified-$u(862)$ are 0.1984 and 0.0957, respectively. The difference between simplified-$u(\lambda)$ and $u(\lambda)$ is $<$0.005%. This shows that $u(\lambda)$ can be replaced by simplified-$u(\lambda)$ with high accuracy in the two NIR bands in order to compute $b_{bp}(\lambda)$ in these two NIR bands using equations (2)–(5).

In equation (4), $b_{bp}(\lambda)$ is spectrally correlated, and generally can be modeled as a function of $b_{bp}(\lambda)$ at a reference wavelength (Gordon & Morel, 1983; IOCCG, 2006), i.e., $b_{bp}(\lambda_0)$, with a power law slope, η. The function can be expressed as

$$b_{bp}(\lambda)=b_{bp}(\lambda_0)\left(\frac{\lambda_0}{\lambda}\right)^{\eta}. \tag{6}$$

In this study, $b_{bp}(745)$ and $b_{bp}(862)$ are derived from VIIRS-measured $nL_w(745)$ and $nL_w(862)$ using the MSL12 with the SWIR atmospheric correction in turbid waters. The power law slope, η, can then be consequently computed from equation (6) with known $b_{bp}(745)$ and $b_{bp}(862)$. With the derived power law slope, η, $b_{bp}(\lambda)$ in the VIIRS visible bands, e.g., $b_{bp}(443)$, $b_{bp}(551)$, can be computed with the reference $b_{bp}(745)$ and the derived power law slope η. Furthermore, the NIR-based $b_{bp}(\lambda)$ scheme is applied to the VIIRS-derived $nL_w(745)$ and $nL_w(862)$, which are generated using the MSL12 SWIR ocean color data processing over the most turbid regions of the global ocean. The spectral features, spatial and temporal variability of $b_{bp}(\lambda)$ for different turbid regions are studied and evaluated.

3. Results

3.1. VIIRS-Derived $nL_w(745)$ and $nL_w(862)$ in Highly Turbid Waters

In highly turbid waters, ocean optical properties are featured with enhanced $nL_w(\lambda)$ in the red and NIR wavelengths (Doron et al., 2011; Doxaran et al., 2002; Shi & Wang, 2014). The turbidity of ocean water is driven by light attenuation in the water column due to the scattering and absorption of the particles and molecules. Thus, the diffuse attenuation coefficient at the wavelength of 490 nm, $K_d(490)$, can be used as a measure of water turbidity to characterize the global ocean turbidity, and to identify the highly turbid regions in the global ocean. Using $K_d(490)$, Shi and Wang (2010b) identified the world's highly turbid regions with MODIS-Aqua observations. Five regions are selected for the highly turbid regions to conduct this study. These regions include (1) China's east coastal region, (2) Amazon River Estuary, (3) La Plata River Estuary, (4) Meghna River Estuary in the Bay of Bengal, and (5) Atchafalaya River Estuary in the distributaries of the Mississippi River.

Figure 2 shows the climatology of VIIRS-derived $nL_w(745)$ (Figures 2a–2e) and $nL_w(862)$ (Figures 2f–2j) between 2012 and 2016 in these five regions. Indeed, these regions feature significantly enhanced $nL_w(745)$ and $nL_w(862)$. Specifically, $nL_w(745)$ and $nL_w(862)$ can reach over ~4–5 and ~2–3 mW cm^{-2} μm^{-1} sr^{-1}, respectively, in some areas of China's east coast region (Figures 2a and 2f) and the Amazon River Estuary (Figures 2b and 2g). Actually, $nL_w(745)$ and $nL_w(862)$ in China's east coastal region show high seasonal variability (Shi & Wang, 2014). In fact, in China's east coastal region $nL_w(745)$ and $nL_w(862)$ during the boreal winter can be above about 5 and 3 mW cm^{-2} μm^{-1} sr^{-1} (not shown here), respectively.

The La Plata River Estuary (Figures 2c and 2h) and the Meghna River Estuary (Figures 2d and 2i) are less turbid than the Amazon River Estuary in terms of $nL_w(745)$ and $nL_w(862)$ magnitudes. In the La Plata River Estuary (Figures 2c and 2h) and the Meghna River Estuary (Figures 2d and 2i), $nL_w(745)$ and $nL_w(862)$ range from

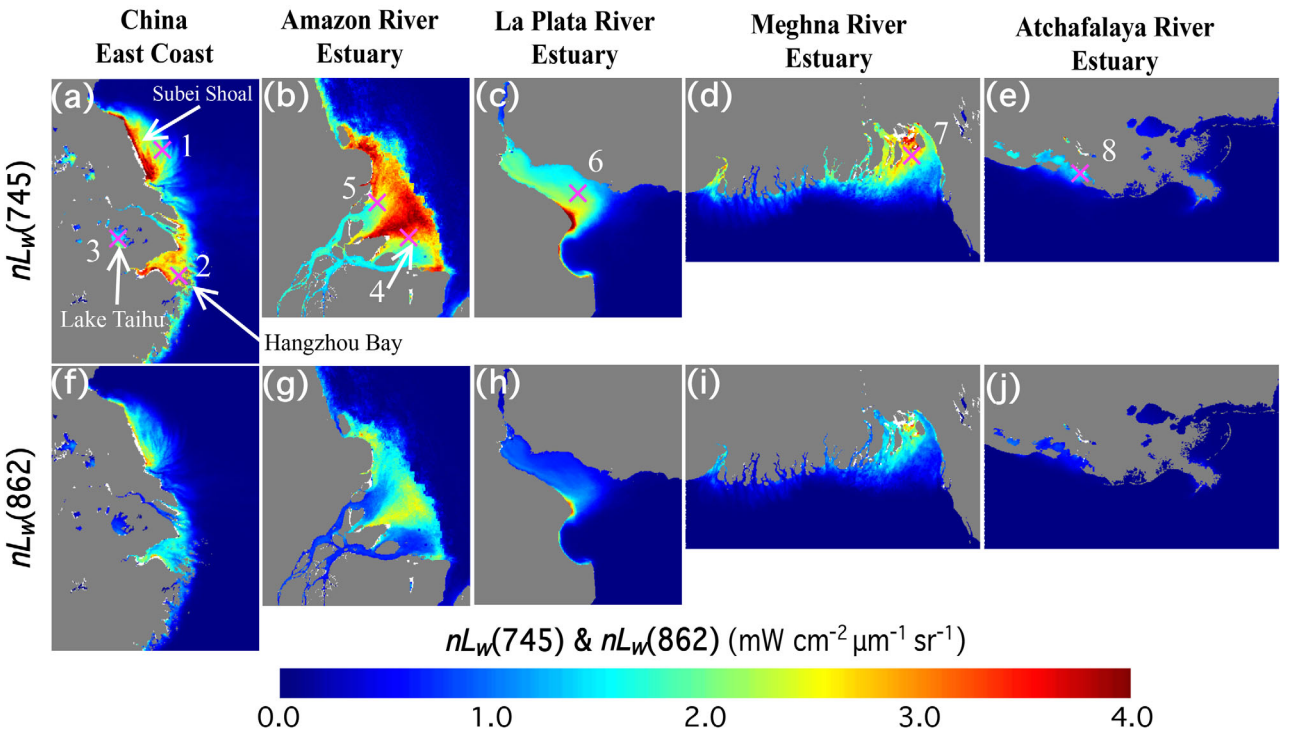

Figure 2. $nL_w(745)$ and $nL_w(862)$ climatology in the regions of (a, f) China's east coastal region between 28.5°N–41.0°N and 115.0°E–127.5°E, (b, g) Amazon River Estuary between 1.0°S–3.0°N and 52.0°W–48.0°W, (c, h) La Plata River Estuary between 37.0°S–33.0°S and 59.0°W–55.0°W, (d, i) Meghna River Estuary between 20.5°N–23.5°N and 87.5°E–92.5°E, and (e, j) Atchafalaya River Estuary between 28.0°N–31.0°N and 93.0°W–88.0°W. Station 1 (33.74°N, 121.26°E), Station 2 (30.36°N, 121.84°E), and Station 3 (31.21°N, 120.14°E) are located in the Subei Shoal, Hangzhou Bay, and Lake Taihu, respectively. Station 4 (0.66°N, 49.11°W) and Station 5 (1.00°N, 49.66°W) are located in the Amazon River Estuary. Station 6 (34.73°S, 57.41°W), Station 7 (22.21°N, 91.40°E), and Station 8 (29.41°N, 91.51°W) are located in the La Plata River Estuary, Meghna River Estuary, and Atchafalaya River Estuary, respectively. These stations are chosen to quantify and evaluate the $b_{bp}(\lambda)$ and their temporal variability in these highly turbid regions. The locations of the Subei Shoal, Hangzhou Bay, and Lake Taihu are also marked in Figure 2a.

~2–4 to ~1–2 mW cm^{-2} μm^{-1} sr^{-1}, respectively. Even though the Atchafalaya River Estuary in distributaries of the Mississippi River is the least turbid water in these five regions, $nL_w(745)$ still ranges from ~1 to 2 mW cm^{-2} μm^{-1} sr^{-1} and $nL_w(862)$ is <~1.0 mW cm^{-2} μm^{-1} sr^{-1}. This is similar to many other coastal and inland turbid regions such as the northern Caspian Sea, the North Sea, and the Chesapeake Bay (Shi & Wang, 2010b).

Overall, the climatology of VIIRS $nL_w(745)$ and $nL_w(862)$ shows that there are significant differences in $nL_w(745)$ and $nL_w(862)$ between highly turbid coastal and inland waters. $nL_w(745)$ can range from ~1 to ~4 mW cm^{-2} μm^{-1} sr^{-1}, and $nL_w(862)$ can range from ~0.5 to ~2.5 mW cm^{-2} μm^{-1} sr^{-1}. The magnitudes of $nL_w(745)$ and $nL_w(862)$ in these highly turbid regions further show that the NIR-based $b_{bp}(\lambda)$ algorithm as proposed in this study can be used to characterize and quantify the particle backscattering of global highly turbid waters from VIIRS ocean color observations.

3.2. Climatology and Seasonal Variability of VIIRS-Derived $b_{bp}(\lambda)$ in the Highly Turbid Waters

3.2.1. China's East Coastal Region

Figure 3 shows the climatology $b_{bp}(\lambda)$ (Figures 3a–3e), $b_{bp}(\lambda)$ in boreal spring (March–May) (Figures 3f–3j), summer (June–August) (Figures 3k–3o), autumn (September–November) (Figures 3p–3t), and winter (December–February) (Figure 3u–3y) derived from VIIRS observations between 2012 and 2016 in the VIIRS bands of 443, 551, 671, 745, and 862 nm. The spatial distributions of $b_{bp}(\lambda)$ are consistent with the spatial patterns of $nL_w(745)$ and $nL_w(862)$. Specifically, enhanced $b_{bp}(\lambda)$ is located in the Subei Shoal, Yangtze River Estuary, and Hangzhou Bay with climatology $b_{bp}(745)$ and $b_{bp}(862)$ over ~2 m^{-1}. In this region, the inland waters such as Lake Taihu also show the enhanced $b_{bp}(\lambda)$ with climatology $b_{bp}(\lambda)$ ~1 m^{-1}.

In addition to the spatial variability of $b_{bp}(\lambda)$ in China's east coastal region, the seasonal variability of the $b_{bp}(\lambda)$ is also significant. Winter season is the most turbid season with enhanced $b_{bp}(\lambda)$ and enlarged

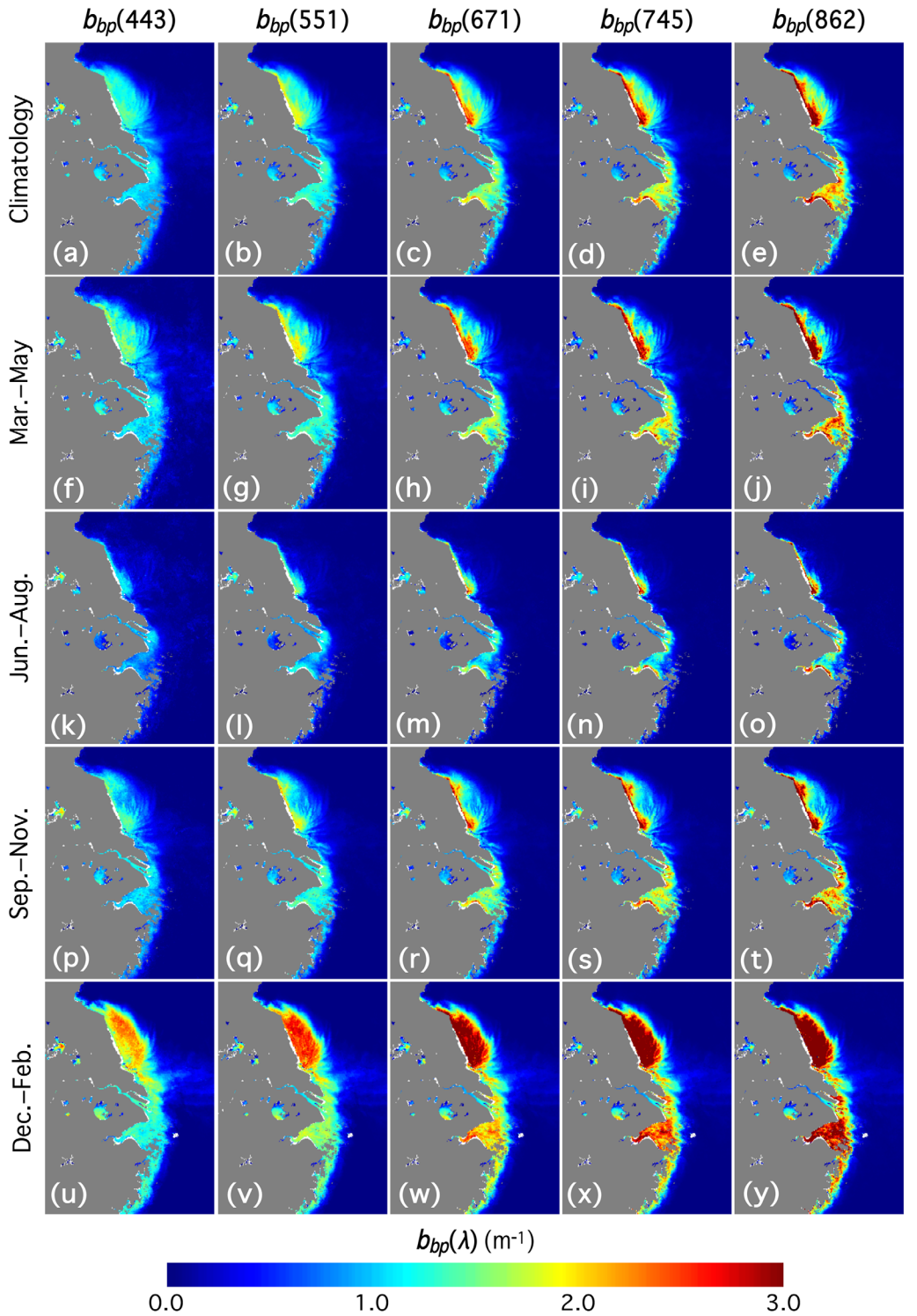

Figure 3. VIIRS-derived images of b_{bp}(443), b_{bp}(551), b_{bp}(671), b_{bp}(745), and b_{bp}(862) in China's east coastal region for (a–e) climatology from 2012 to 2016, (f–j) March–May (spring), (k–o) June–August (summer), (p–t) September–November (fall), and (u–y) December–February (winter).

coverage of high $b_{bp}(\lambda)$ in China's east coastal region (Figures 3u–3y). In the Subei Shoal and Hangzhou Bay, b_{bp}(745) and b_{bp}(862) can reach above $\sim$3 m^{-1}. In contrast, the lowest $b_{bp}(\lambda)$ occurs in the summer season (Figures 3k–3o). In most of the coastal turbid regions $b_{bp}(\lambda)$ drops to $<\sim$1 m^{-1}. In the spring (Figures 3f–3j)

and autumn (Figures 3p–3t), $b_{bp}(\lambda)$ are similar to each other in terms of magnitude values and spatial distributions.

Figure 3 also shows that $b_{bp}(\lambda)$ spectral changes are regional-dependent and seasonal-dependent. It is noted that $b_{bp}(\lambda)$ in the visible is not derived from $R_{rs}(\lambda)$ directly, instead it is analytically estimated based on $b_{bp}(\lambda)$ in the NIR bands and the power law slope, η, using equation (6). In Lake Taihu, $b_{bp}(\lambda)$ is more or less flat for all the seasons from $b_{bp}(443)$ to $b_{bp}(862)$. However, $b_{bp}(\lambda)$ increases with the wavelength for highly turbid waters such as in the Subei Shoal and Hangzhou Bay. Indeed, $b_{bp}(\lambda)$ increases from $\sim$2 m^{-1} at 443 nm to over $\sim$3 m^{-1} in the Subei Shoal during the winter season (Figures 3u–3y). On the other hand, $b_{bp}(\lambda)$ decreases from 443 to 862 nm in some parts of China's east coastal region. As an example, $b_{bp}(\lambda)$ drops from $\sim$1.5 m^{-1} at 443 nm to $<$1.0 m^{-1} at 745 nm in the far offshore outskirts of the Subei Shoal plume during the spring season (Figures 3f–3j).

3.2.2. Amazon River Estuary

As the most turbid waters in the global ocean, the Amazon River Estuary is featured with enhanced $b_{bp}(\lambda)$ for all four seasons. Figure 4 shows the climatology $b_{bp}(\lambda)$ (Figures 4a–4e), $b_{bp}(\lambda)$ in the season from months

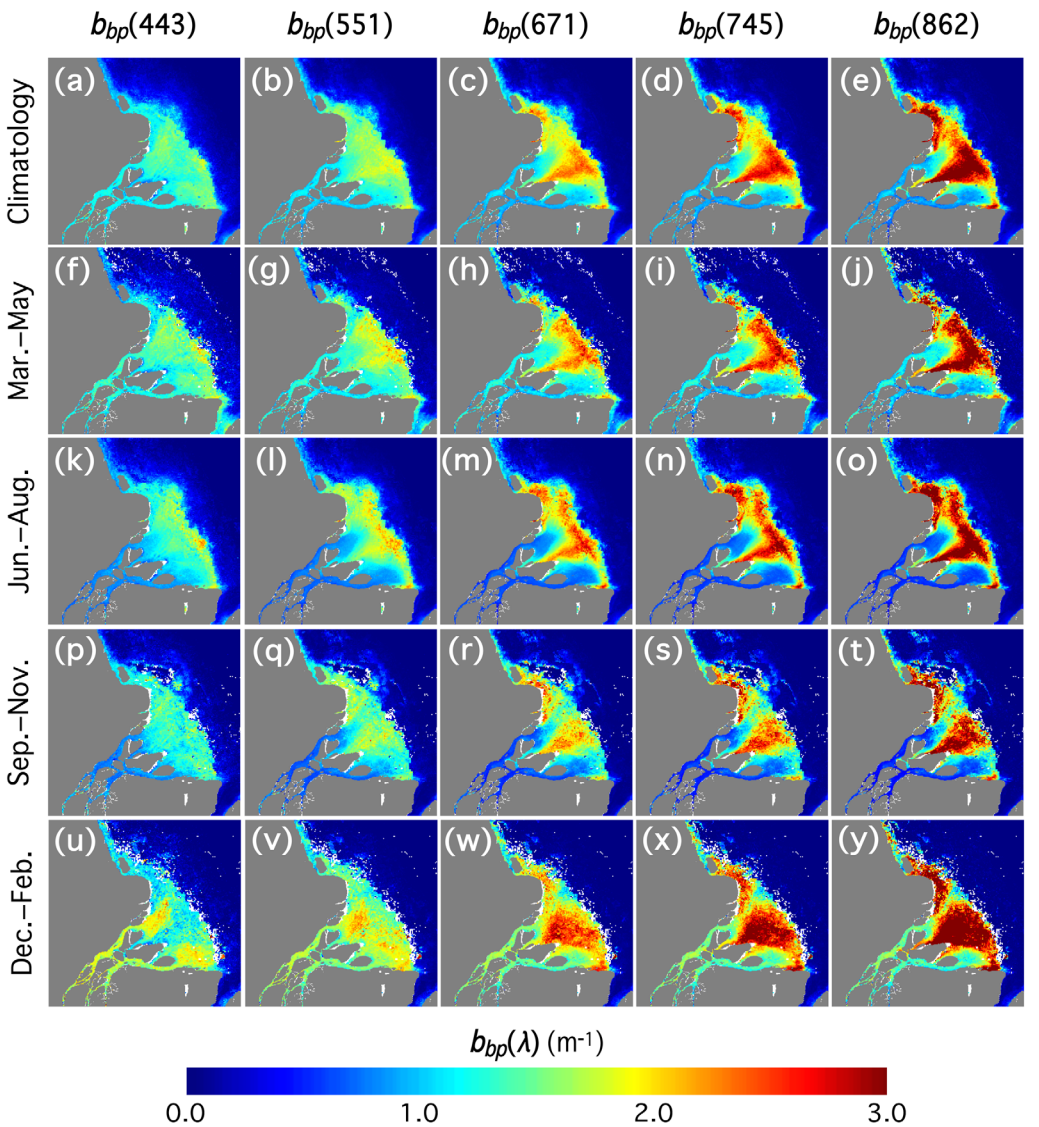

Figure 4. VIIRS-derived images of $b_{bp}(443)$, $b_{bp}(551)$, $b_{bp}(671)$, $b_{bp}(745)$, and $b_{bp}(862)$ in the Amazon River Estuary for (a–e) climatology from 2012 to 2016, (f–j) March–May, (k–o) June–August, (p–t) September–November, and (u–y) December–February.

of March–May (Figures 4f–4j), June–August (Figures 4k–4o), September–November (Figures 4p–4t), and December–February (Figures 4u–4y). $b_{bp}(862)$ is over ~3–4 m^{-1} in the large portion of the Amazon River Estuary. Different from China's east coastal region, there is no significant seasonal variation of $b_{bp}(\lambda)$ in this region. Conversely, the $b_{bp}(\lambda)$ spectral shape changes with regions depending on the magnitude of $b_{bp}(\lambda)$. This is similar to China's east coastal region. In the highly turbid part of the Amazon River Estuary, such as the central Amazon River Estuary, $b_{bp}(\lambda)$ increases with the wavelength between 443 and 862 nm. However, in the less turbid waters such as the regions in the south and north branches of the Amazon River, $b_{bp}(\lambda)$ decreases or stays flat with the wavelength between 443 and 862 nm.

3.2.3. La Plata River Estuary

Figure 5 shows another highly turbid region of the La Plata River Estuary. The climatology $b_{bp}(443)$ shows that its value is ~1.5–2.0 m^{-1} for the most part of the La Plata River Estuary (Figure 5a). $b_{bp}(\lambda)$ decreases from $b_{bp}(443)$ to $b_{bp}(862)$ with climatology $b_{bp}(862)$ ~0.5–1.0 m^{-1} (Figure 5e). Unlike the Amazon River Estuary, seasonal variability of the $b_{bp}(\lambda)$ can be found in the La Plata River Estuary. The highest $b_{bp}(\lambda)$ occurs in the months of March–May (Figures 5f–5j), i.e., the Australia fall season. $b_{bp}(443)$ is ~3 m^{-1} for most parts of the La Plata River Estuary, while the climatology $b_{bp}(443)$ is generally <~2 m^{-1}. For the other seasons

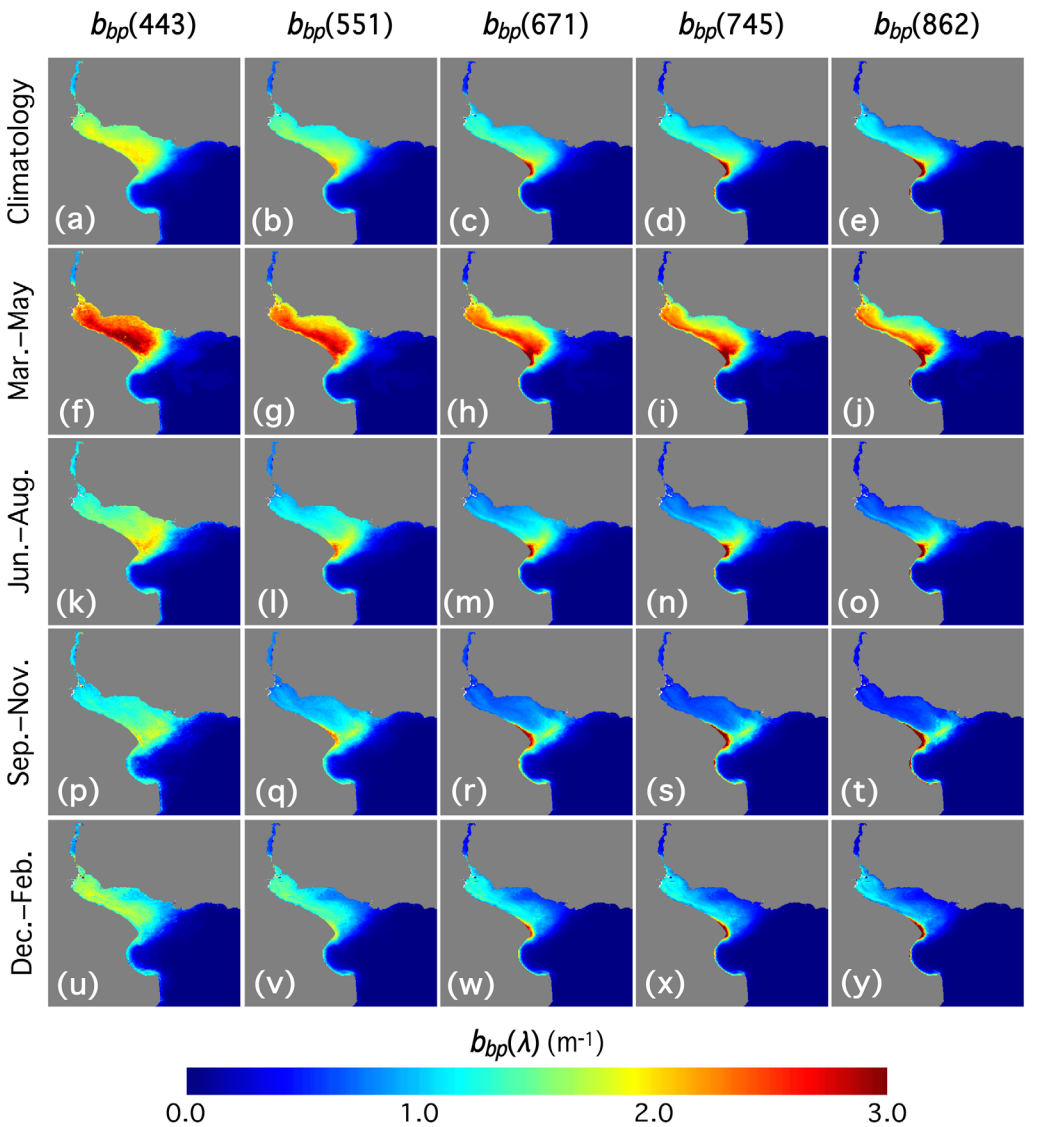

Figure 5. VIIRS-derived images of $b_{bp}(443)$, $b_{bp}(551)$, $b_{bp}(671)$, $b_{bp}(745)$, and $b_{bp}(862)$ in the La *Plata* River Estuary for (a–e) climatology from 2012 to 2016, (f–j) March–May, (k–o) June–August, (p–t) September–November, and (u–y) December–February.

(Australian spring, summer, and winter), $b_{bp}(\lambda)$ in the La Plata River Estuary is moderately high with a typical $b_{bp}(\lambda)$ in these seasons only half of $b_{bp}(\lambda)$ values in the Australian fall. The seasonal variation in $b_{bp}(\lambda)$ for the Australian spring, summer, and winter is also generally less significant.

In China's east coastal region and the Amazon River Estuary, the $b_{bp}(\lambda)$ spectral shape generally depends on the values of $b_{bp}(\lambda)$. $b_{bp}(\lambda)$ increases with the wavelength for high $b_{bp}(\lambda)$ values (e.g., $b_{bp}(862) \sim 2$–$3\ m^{-1}$) and decreases or becomes flat in the regions with moderately high $b_{bp}(\lambda)$ (e.g., $b_{bp}(\lambda) \sim 1.0\ m^{-1}$). However, in the La Plata River Estuary, $b_{bp}(\lambda)$ decreases with the wavelength for all types of waters. In the Australian fall season, the $b_{bp}(\lambda)$ decreases from $\sim 3\ m^{-1}$ in $b_{bp}(443)$ (Figure 5f) to $\sim 2\ m^{-1}$ in $b_{bp}(862)$ (Figure 5j) for most parts of the La Plata River Estuary. This optical property difference of $b_{bp}(\lambda)$ in the region suggests that the physical and biogeochemical properties of minerals in the water column of the La Plata River Estuary are different from those of the other two regions.

3.2.4. Meghna River Estuary

Climatology of $b_{bp}(\lambda)$ (Figures 6a–6e) and seasonal $b_{bp}(\lambda)$ are shown in Figure 6. In this region, the seasonal variation of $b_{bp}(\lambda)$ is significant with peak $b_{bp}(\lambda)$ occurring in the boreal summer and autumn seasons. This might be attributed to the seasonal monsoon and high rainfall and river flow in these two seasons. At the mouth the Meghna River, $b_{bp}(862)$ can reach $\sim 3\ m^{-1}$ in the autumn. In the Meghna River Estuary, $b_{bp}(\lambda)$ increases with the wavelength for regions with $b_{bp}(862)$ over $\sim 2\ m^{-1}$ in the summer and autumn seasons. However, $b_{bp}(\lambda)$ also increases with the wavelength for regions with $b_{bp}(862) < \sim 2\ m^{-1}$ in the other seasons. The same $b_{bp}(\lambda)$ spectral variations for both highly turbid waters ($b_{bp}(862) \sim 2$–$3\ m^{-1}$) and moderately turbid waters ($b_{bp}(862) < \sim 2\ m^{-1}$) in this region are different from the $b_{bp}(\lambda)$ spectral variation in China's

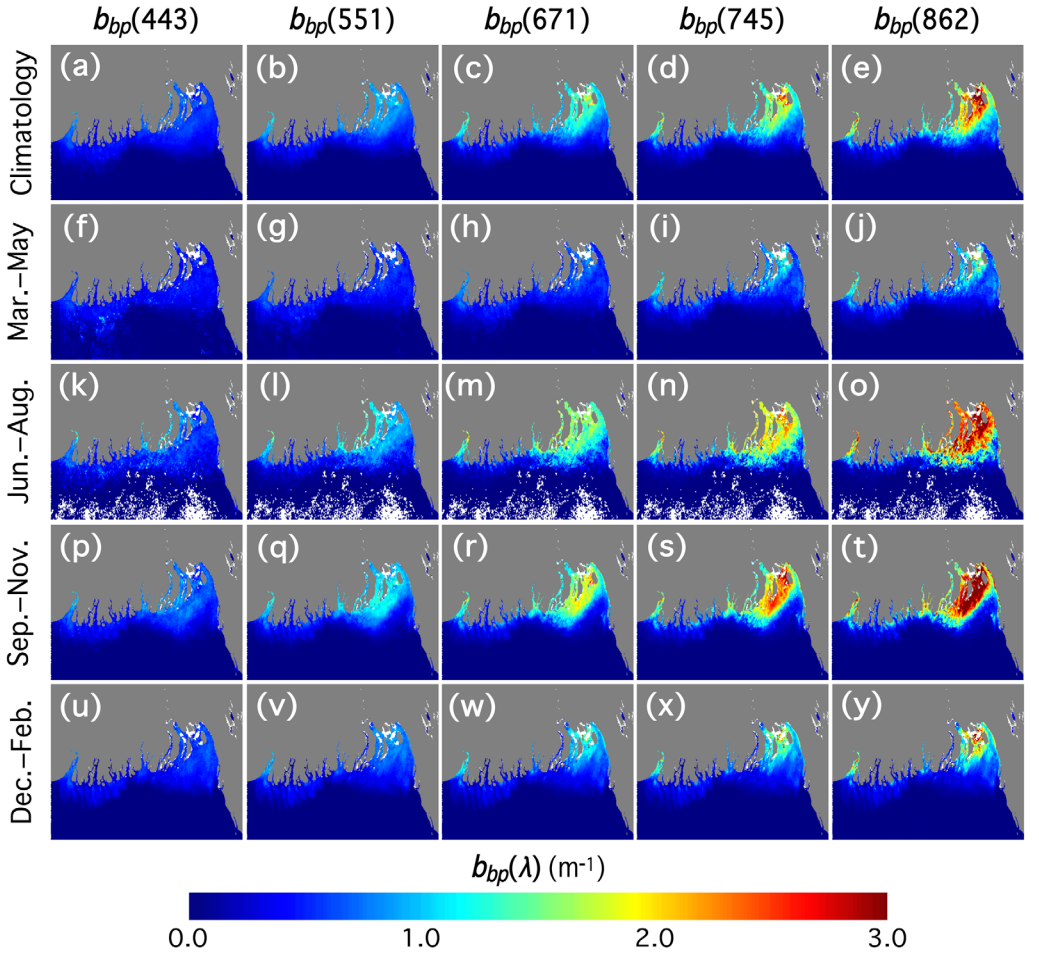

Figure 6. VIIRS-derived images of $b_{bp}(443)$, $b_{bp}(551)$, $b_{bp}(671)$, $b_{bp}(745)$, and $b_{bp}(862)$ in the Meghna River Estuary for (a–e) climatology from 2012 to 2016, (f–j) March–May, (k–o) June–August, (p–t) September–November, and (u–y) December–February.

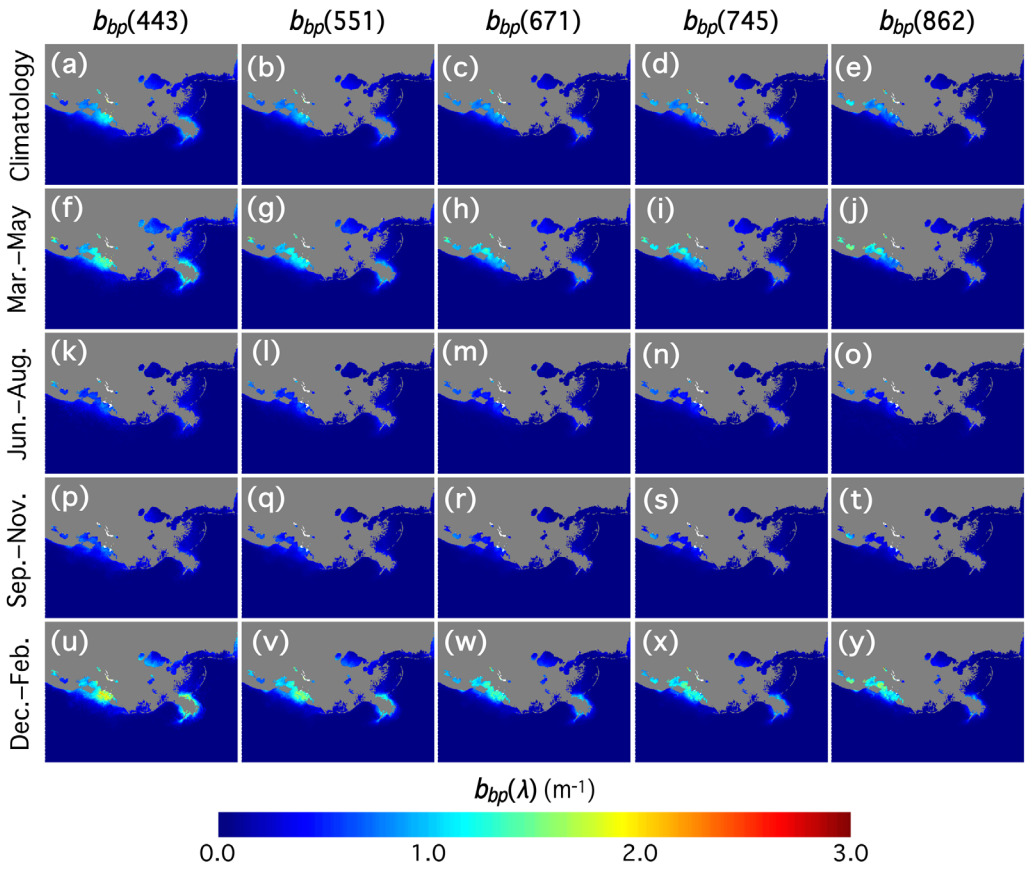

Figure 7. VIIRS-derived images of b_{bp}(443), b_{bp}(551), b_{bp}(671), b_{bp}(745), and b_{bp}(862) in the Mississippi River Estuary and Atchafalaya River Estuary for (a–e) climatology from 2012 to 2016, (f–j) March–May, (k–o) June–August, (p–t) September–November, and (u–y) December–February.

east coastal region (Figure 3) and the Amazon River Estuary (Figure 4) where $b_{bp}(\lambda)$ spectral variations depend on the values of $b_{bp}(\lambda)$.

3.2.5. Atchafalaya River Estuary and Mississippi River Estuary

In comparison with the highly turbid regions shown previously, the Atchafalaya River Estuary is a moderately turbid region in terms of $b_{bp}(\lambda)$ values. This region is chosen for analysis because it is a typical turbid region similar to the other turbid regions such as the Chesapeake Bay, the North Sea, and the Northern Caspian Sea (Shi & Wang, 2010b), and the ecosystem of this region is complex and dynamic.

Figure 7 shows the climatology of $b_{bp}(\lambda)$ (Figures 7a–7e) and seasonal $b_{bp}(\lambda)$ in the Atchafalaya River Estuary and Mississippi River Estuary. Seasonal variation in $b_{bp}(\lambda)$ is also significant with high $b_{bp}(\lambda)$ in the boreal spring (Figures 7f–7j) and winter (Figures 7u–7y). Low $b_{bp}(\lambda)$ can be found in summer (Figures 7k–7o) and autumn (Figures 7p–7t). In the boreal winter, b_{bp}(443) can reach ~1.5–2 m^{-1} in the Atchafalaya River Estuary (Figure 7u). b_{bp}(862) in the winter is ~1.0–1.5 m^{-1} (Figure 7y). In the summer season, however, $b_{bp}(\lambda)$ drops to about half of the $b_{bp}(\lambda)$ in the winter season.

3.2.6. Spectral Variation of $b_{bp}(\lambda)$ in the Highly Turbid Regions

Figures 3–7 show different $b_{bp}(\lambda)$ spectral features in these five turbid regions. Figure 8 further characterizes and quantifies the $b_{bp}(\lambda)$ variations with the wavelength at the different stations marked in Figure 2. Stations 1–3 in the Subei Shoal, Hangzhou Bay, and Lake Taihu are located in China's east coastal region. Stations 4 and 5 are located in the Amazon River Estuary. Stations 6–8 are located in the La Plata River Estuary, Meghna River Estuary, and Atchafalaya River Estuary, respectively.

In general, all of the $b_{bp}(\lambda)$ at these eight stations for different seasons are highly dynamic. $b_{bp}(\lambda)$ can range from <~0.5 m^{-1} to over ~2–3 m^{-1}. The $b_{bp}(\lambda)$ spectra can increase or decrease with the wavelength depending on the regions and the seasons. At Station 1 in the Subei Shoal, $b_{bp}(\lambda)$ is only ~0.2–0.3 m^{-1} in

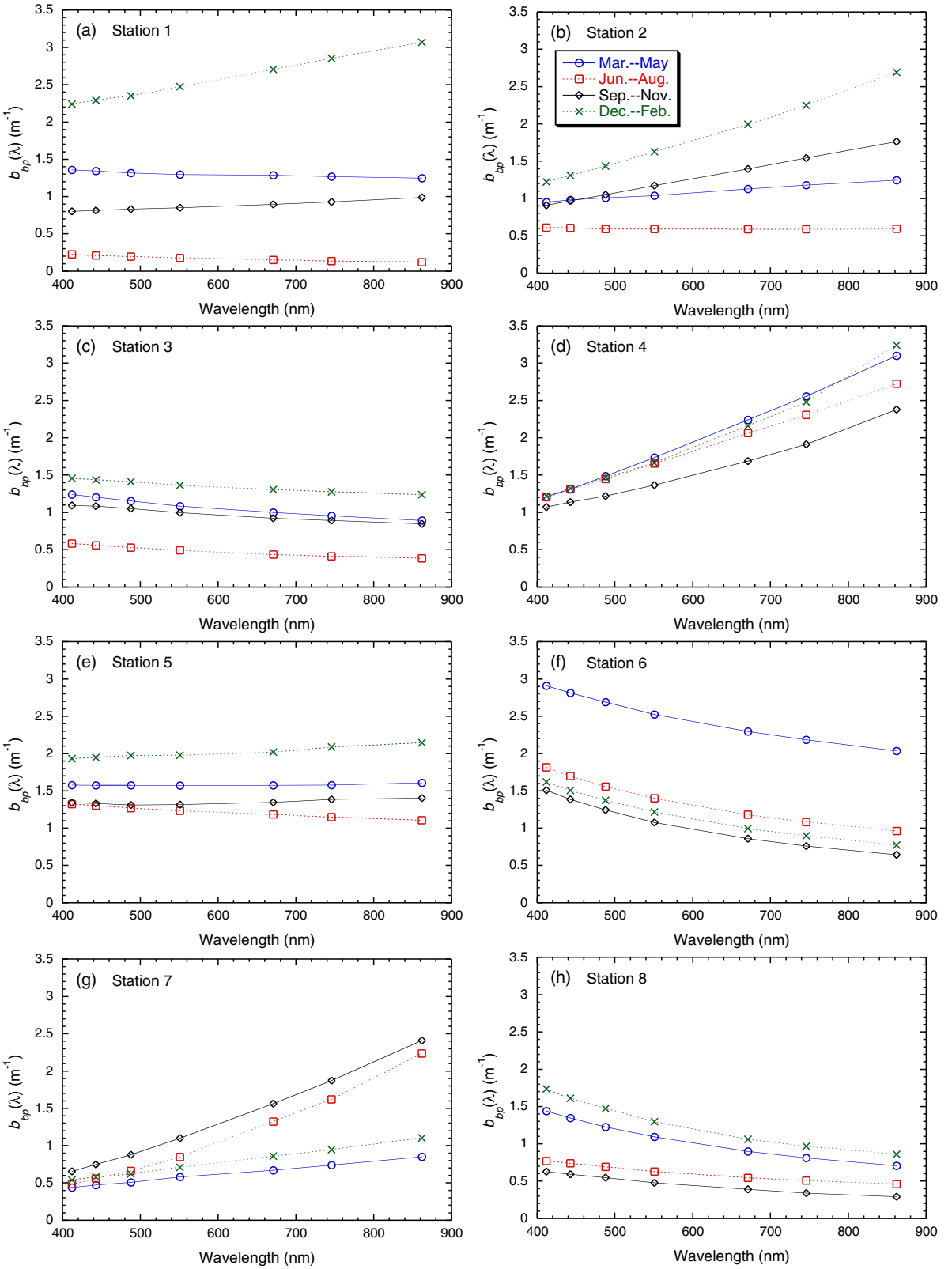

Figure 8. The $b_{bp}(\lambda)$ spectral variations in different seasons at (a) Station 1 in the Subei Shoal, (b) Station 2 in the Hangzhou Bay, (c) Station 3 in the Lake Taihu, (d) Station 4 in the Amazon River Estuary, (e) Station 5 in the Amazon River Estuary, (f) Station 6 in the La Plata River Estuary, (g) Station 7 in the Meghna River Estuary, and (h) Station 8 in the Atchafalaya River Estuary.

the boreal summer, while $b_{bp}(\lambda)$ reaches ~2–3 m^{-1} in the boreal winter (Figure 8a). At Station 2 in the Hangzhou Bay, $b_{bp}(\lambda)$ variations are similar to the $b_{bp}(\lambda)$ at Station 1. In Lake Taihu, $b_{bp}(\lambda)$ is less than those at both Stations 1 and 2. In fact, $b_{bp}(\lambda)$ spectra are generally flat for all four seasons (Figure 8c).

Figure 8d shows less seasonality of $b_{bp}(\lambda)$ in the highly turbid region of the Amazon River Estuary. For all four seasons, $b_{bp}(\lambda)$ increases with increase of the wavelength for $b_{bp}(862)$ above ~2 m^{-1} for all four seasons at Station 4. In contrast, $b_{bp}(\lambda)$ spectra are generally flat in all four seasons at Station 5 (Figure 8e). In the La Plata River Estuary (Figure 8f), $b_{bp}(\lambda)$ spectra decrease with increase of the wavelength even though $b_{bp}(\lambda)$ values are similar to those in the highly turbid waters of China's east coastal region and the Amazon River Estuary. In the Meghna River Estuary (Figure 8g), $b_{bp}(\lambda)$ spectra are similar to those at Station 4 during the boreal summer and autumn, and $b_{bp}(\lambda)$ spectra slightly increase with increase of the wavelength in the boreal winter and spring.

In summary, $b_{bp}(\lambda)$ can be over ~2 m^{-1} for most of the highly turbid waters shown in this study. The $b_{bp}(\lambda)$ trends high with the increase of the wavelength at Stations 1, 2, 4, 6, and 7. On the other hand, $b_{bp}(\lambda)$ is generally flat in the visible and NIR bands at Station 3 in Lake Taihu, and at Station 5 in moderately turbid waters in the Amazon River Estuary. At Station 6 in the La Plata River Estuary and Station 8 in the Atchafalaya River Estuary, $b_{bp}(\lambda)$ decreases with increase of the wavelength for all four seasons.

3.3. Interannual Variability of VIIRS-Derived $b_{bp}(\lambda)$ in Highly Turbid Waters

The time series of $b_{bp}(\lambda)$ at these eight stations are shown in Figure 9. Remarkable seasonal cycles of $b_{bp}(\lambda)$ can be found in the Subei Shoal (Station 1), Hangzhou Bay (Station 2), and Lake Taihu (Station 3). At Station 1, $b_{bp}(\lambda)$ ranges from ~0.2–0.3 m^{-1} in the boreal summer to ~3–4 m^{-1} in the boreal winter. This represents a seasonal expansion and reduction of the sediment plumes in the Subei Shoal (Shi & Wang, 2012a). In the Hangzhou Bay, $b_{bp}(\lambda)$ experiences more interannual variability than those in the Subei Shoal. Indeed, in the 2013–2014 winter (December–February), $b_{bp}(862)$ reached over ~4 m^{-1}

Figures 9d and 9e show that no significant seasonal $b_{bp}(\lambda)$ variation for both moderately and highly turbid waters. Peak $b_{bp}(\lambda)$ generally occurs in the months of December–February. The enhanced $b_{bp}(\lambda)$ can be attributed to the downpour rainfall and flooding rivers in this rainy season (Zeng, 1999). In the La Plata River Estuary (Figure 9f), the interannual variation of $b_{bp}(\lambda)$ is also significant in addition to the seasonal change. In the Australian fall (March–May) of 2012, $b_{bp}(\lambda)$ reached over ~4 m^{-1}, while $b_{bp}(\lambda)$ was ~1–2 m^{-1} for the other years. At Station 7 in the Meghna River Estuary, a seasonal change of $b_{bp}(\lambda)$ can also be found with peak values in the boreal summer and autumn seasons. However, interannual changes of $b_{bp}(\lambda)$ are still significant (Figure 9g). In the Atchafalaya River Estuary (Figure 9h), the $b_{bp}(\lambda)$ ranges between ~0.3–0.5 m^{-1} in the boreal summer and ~1.0–1.5 m^{-1} in the boreal winter. $b_{bp}(\lambda)$ in this region is similar to that in Lake Taihu (Figure 9h).

3.4. Combination of the NIR-Based and QAA-Based $b_{bp}(\lambda)$ Algorithm

In this study, the NIR-based $b_{bp}(\lambda)$ algorithm can be applied to seasonal and climatology VIIRS $nL_w(745)$ and $nL_w(862)$ for retrieving $b_{bp}(\lambda)$ in the entire visible and NIR spectrum for coastal and inland waters. However, in open oceans and less turbid waters, water is generally black at the NIR wavelengths. Thus, $nL_w(745)$ and $nL_w(862)$ are close to 0. Equations (1)–(6) for the NIR-based $b_{bp}(\lambda)$ algorithm show that the algorithm is sensitive to the ratio of $b_{bp}(745)/b_{bp}(862)$, which is proportional to the ratio of $nL_w(745)/nL_w(862)$. This suggests that a small error in satellite-derived $nL_w(745)$ and $nL_w(862)$ can result in a significant error in $b_{bp}(\lambda)$ over the clear open ocean waters. Conversely, in turbid waters, $b_{bp}(\lambda)$ is much less sensitive to small errors in satellite-derived $nL_w(745)$ and $nL_w(862)$ due to enhanced signals of $nL_w(745)$ and $nL_w(862)$.

In this study, VIIRS $nL_w(745)$ and $nL_w(862)$ are derived from the SWIR-based atmospheric correction using VIIRS SWIR bands M8 and M10 (1,238 and 1,601 nm). The low signal-to-noise-ratio (SNR) for these two SWIR bands determines that $nL_w(745)$ and $nL_w(862)$ retrievals in the open ocean can be noisy and less accurate (Wang & Shi, 2012), even though indeed the VIIRS $nL_w(\lambda)$ products from the SWIR atmospheric correction are generally consistent with those from the NIR-based atmospheric correction algorithm (Wang et al., 2016a, 2016b).

Figures 10a–10e show the climatology NIR-based $b_{bp}(\lambda)$ in China's east coastal region. To enhance the $b_{bp}(\lambda)$ for a better evaluation in the open ocean, a log scale is used in Figure 10. Indeed, using the NIR-based approach $b_{bp}(\lambda)$ images in the open oceans shows high noise levels especially for $b_{bp}(443)$ (Figure

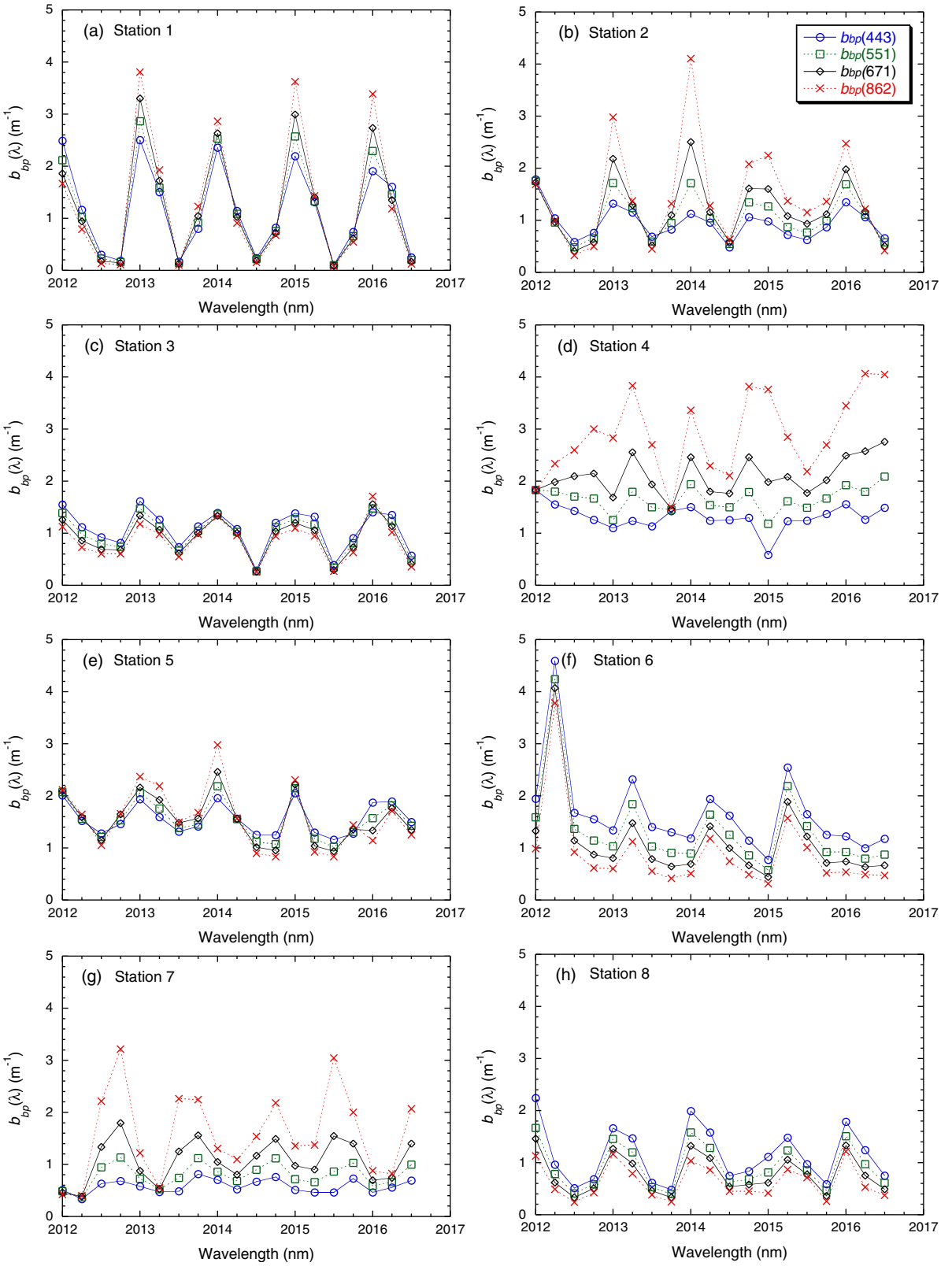

Figure 9. Interannual variations of VIIRS-derived $b_{bp}(443)$, $b_{bp}(551)$, $b_{bp}(671)$, and $b_{bp}(862)$ at (a) Station 1 in the Subei Shoal, (b) Station 2 in the Hangzhou Bay, (c) Station 3 in the Lake Taihu, (d) Station 4 in the Amazon River Estuary, (e) Station 5 in the Amazon River Estuary, (f) Station 6 in the La Plata River Estuary, (g) Station 7 in the Meghna River Estuary, and (h) Station 8 in the Atchafalaya River Estuary.

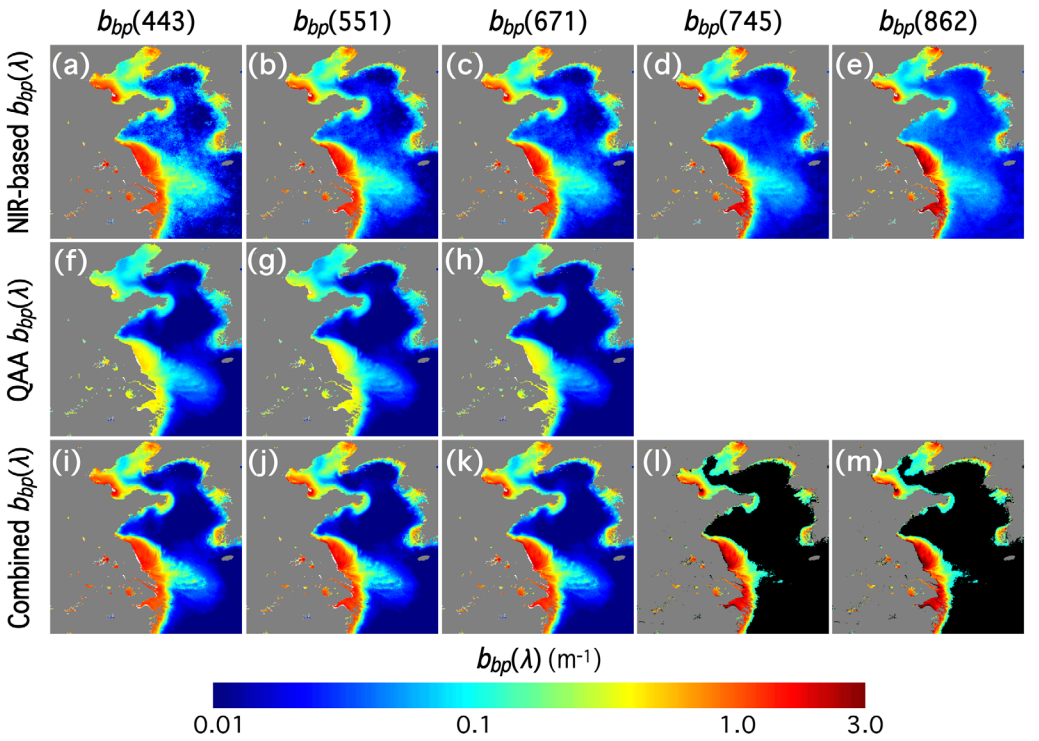

Figure 10. VIIRS climatology $b_{bp}(\lambda)$ derived from the approaches of (a–e) the NIR-based $b_{bp}(\lambda)$ algorithm, (f–h) the QAA-based $b_{bp}(\lambda)$ algorithm, and (i–m) the NIR-QAA combined $b_{bp}(\lambda)$ algorithm.

10a). As described in equations (1)–(6), b_{bp}(443) (Figure 10a), b_{bp}(551) (Figure 10b), and b_{bp}(671) (Figure 10c) are all derived from b_{bp}(745) (Figure 10d) and b_{bp}(862) (Figure 10e) with the NIR-based algorithm. Figures 10f–10h show the climatology QAA (Version 5) $b_{bp}(\lambda)$ at 443, 551, and 671 nm along China's east coastal region for comparison. In general, QAA-derived $b_{bp}(\lambda)$ products are smooth and less noisy for the entire region. Note that there are no b_{bp}(745) and b_{bp}(862) products from the QAA-based algorithm. In the open ocean, QAA-derived $b_{bp}(\lambda)$ products are not only smooth, but also smaller in comparison with those from the NIR-based $b_{bp}(\lambda)$ algorithm. This further shows that the NIR-based $b_{bp}(\lambda)$ in the open ocean can be noisy and even might be invalid due to the low SNR at the SWIR bands and the less accurate nL_w(745) and nL_w(862) retrievals (almost no signals).

It is also noted that QAA-based $b_{bp}(\lambda)$ in highly turbid waters (Figures 10f–10h) in the visible bands is ~4–5 times less than those from the corresponding NIR-based $b_{bp}(\lambda)$ algorithm (Figures 10a–10c). The QAA IOP algorithm is more or less developed for open oceans and less turbid waters. Specifically, power law slope, η, is estimated from nL_w(443) and nL_w(551) empirically. Multiple studies (Shi & Wang, 2009b, 2014) have shown that $nL_w(\lambda)$ can be saturated in the visible bands in highly turbid coastal and inland waters. This implies that the QAA algorithm underestimates the $b_{bp}(\lambda)$ and even loses its sensitivity to the $b_{bp}(\lambda)$ change in the moderately to highly turbid waters. In contrast, the NIR-based algorithm can perform well in the moderately to highly turbid waters where the NIR $nL_w(\lambda)$ have significant contributions. This is because the NIR $nL_w(\lambda)$ can be highly correlated to the $b_{bp}(\lambda)$ and the errors in $nL_w(\lambda)$ derived from the SWIR-based atmospheric correction are insignificant in comparison with the enhanced NIR $nL_w(\lambda)$.

The advantages and disadvantages of the QAA-based and NIR-based $b_{bp}(\lambda)$ algorithms suggest that these two algorithms complement each other. Thus, a combined $b_{bp}(\lambda)$ is preferable in order to derive accurate $b_{bp}(\lambda)$ products for both the open ocean and turbid coastal/inland waters. Similar to the approach to the NIR-SWIR atmospheric correction algorithm, which combines the NIR-based and SWIR-based atmospheric correction algorithms for the open ocean and turbid coastal/inland waters (Wang & Shi, 2007), we propose a scheme for this combined $b_{bp}(\lambda)$ algorithm after extensive tests and evaluations. Since turbid waters are always featured with an enhanced nL_w(745) value, and nL_w(745) is a direct optical retrieval product in the satellite ocean color data processing, nL_w(745) is used to determine which $b_{bp}(\lambda)$ algorithm is used in

producing VIIRS $b_{bp}(\lambda)$ data. A combined scheme has been developed and can be easily implemented into the MSL12 ocean color data processing. This scheme is outlined as follows:

1. for $nL_w(745) \le 0.1$ mW cm^{-2} μm^{-1} sr^{-1}, $b_{bp}(\lambda) = b_{bp}^{(QAA)}(\lambda)$
2. for $0.1 < nL_w(745) < 0.2$ mW cm^{-2} μm^{-1} sr^{-1}

$$b_{bp}(\lambda) = b_{bp}^{(QAA)}(\lambda) + (10\, nL_w(745) - 1) \times (b_{bp}^{(NIR)}(\lambda) - b_{bp}^{(QAA)}(\lambda))$$

3. for $nL_w(745) \ge 0.2$ mW cm^{-2} μm^{-1} sr^{-1}, $b_{bp}(\lambda) = b_{bp}^{(NIR)}(\lambda)$,

where $b_{bp}{}^{(QAA)}(\lambda)$ and $b_{bp}{}^{(NIR)}(\lambda)$ are from the QAA-based and NIR-based $b_{bp}(\lambda)$ algorithm. However, it is obvious that, for $b_{bp}(\lambda)$ data at the NIR bands, they can only be produced using the NIR-based $b_{bp}(\lambda)$ method. Figures 10i–10k show results of the combined VIIRS climatology $b_{bp}(\lambda)$ data for the b_{bp}(443) (Figure 10i), b_{bp}(551) (Figure 10j), and b_{bp}(671) (Figure 10k), respectively. Since there are no QAA b_{bp}(745) and b_{bp}(862) data, combined b_{bp}(745) (Figure 10l) and b_{bp}(862) (Figure 10m) only show the areas with $nL_w(745) \ge 0.2$ mW cm^{-2} μm^{-1} sr^{-1}. In comparison with the NIR-based climatology $b_{bp}(\lambda)$, the combined $b_{bp}(\lambda)$ products show significant improvements in the open ocean. In coastal and inland water regions, values of combined $b_{bp}(\lambda)$ become much higher than those from the QAA approach. Furthermore, no discontinuity can be found in the transition zones from the QAA $b_{bp}(\lambda)$ in the open ocean to the NIR-based $b_{bp}(\lambda)$ in the turbid coastal waters. This demonstrates that this scheme can provide the best quality of $b_{bp}(\lambda)$ products for both the open ocean and turbid coastal/inland waters.

4. Discussion

Satellite-derived $nL_w(\lambda)$ spectra are determined by the water IOP properties of the four components in the water column, i.e., pure water, phytoplankton, CDOM, and minerals. In the open ocean, pure water, Chl-a, and CDOM are the dominant components (Garver & Siegel, 1997; Hoge & Lyon, 1996; Lee et al., 2002; Werdell et al., 2013). Thus, water IOP properties can be derived with good accuracy from $nL_w(\lambda)$ in the visible wavelength. However, in complex turbid coastal and inland waters, minerals can play a significant role in determining the $nL_w(\lambda)$ spectra (Gordon & Morel, 1983). The dynamic optical and biogeochemical features of minerals make it very challenging to retrieve accurate IOPs in turbid coastal and inland waters.

In this study, we have demonstrated that the $b_{bp}(\lambda)$ algorithm can generally be significantly simplified at the NIR wavelengths in the turbid coastal and inland waters. Thus, $b_{bp}(\lambda)$ at the two NIR bands can be computed directly, and furthermore, $b_{bp}(\lambda)$ in the visible can be computed analytically. This approach shows advantages over the other $b_{bp}(\lambda)$ algorithms such as QAA (Lee et al., 2002), GSM (Garver & Siegel, 1997), and GIOP (Werdell et al., 2013) for turbid coastal and inland waters since no empirical formula is used in this algorithm and it can also avoid a possible $nL_w(\lambda)$ saturation issue in the visible over highly turbid waters (Shi & Wang, 2014).

Indeed, the NIR-based $b_{bp}(\lambda)$ algorithm is able to derive reasonably accurate $b_{bp}(\lambda)$ data in turbid coastal and inland waters. The comparison between the $b_{bp}(\lambda)$ derived using the NIR-based algorithm and the IOCCG synthesized data set for IOP algorithm developments (IOCCG, 2006) shows that error in $b_{bp}(\lambda)$ retrievals at the 440, 550, 670, and 800 nm is $<\sim$2% in waters with $K_d(490) > 1.0$ m^{-1}. In China's east coastal region, VIIRS-derived $b_{bp}(\lambda)$ images (Figure 3) in the spring are qualitatively consistent with the in situ $b_{bp}(\lambda)$ measurements (Zhang et al., 2010a). In turbid waters such as the Subei Shoal region, VIIRS $b_{bp}(\lambda)$ is $\sim$1–2 m^{-1}, consistent with the in situ $b_{bp}(\lambda)$ observations. In contrast, QAA-derived $b_{bp}(\lambda)$ data (not shown here) are significantly lower than those from in situ observations in the turbid China's east coastal region. In Lake Taihu, VIIRS-derived $b_{bp}(\lambda)$ is $\sim$1.0 m^{-1} during the autumn season, and the $b_{bp}(\lambda)$ spectrum is relatively flat. This also qualitatively agrees with in situ measurements (Ma et al., 2009).

On the other hand, field experiments in the Elbe and Gironde River Estuaries in Europe show the scattering coefficient $b_p(\lambda)$ closely matches the power law relationship with the wavelength λ in the NIR wavelengths and the power law slope η is generally consistent with the $b_p(\lambda)$ power law slope in the visible. Stramski et al. (2007) also show that $b_p(\lambda)$ spectra are also wavelength dependent and follow the power law of the wavelength ($\sim\lambda^{-\eta}$). This suggests that $b_{bp}(\lambda)$ ($b_p(\lambda)$ $\times$ backscattering ratio) in the entire spectra can be derived with known $b_{bp}(\lambda)$ at the two NIR bands.

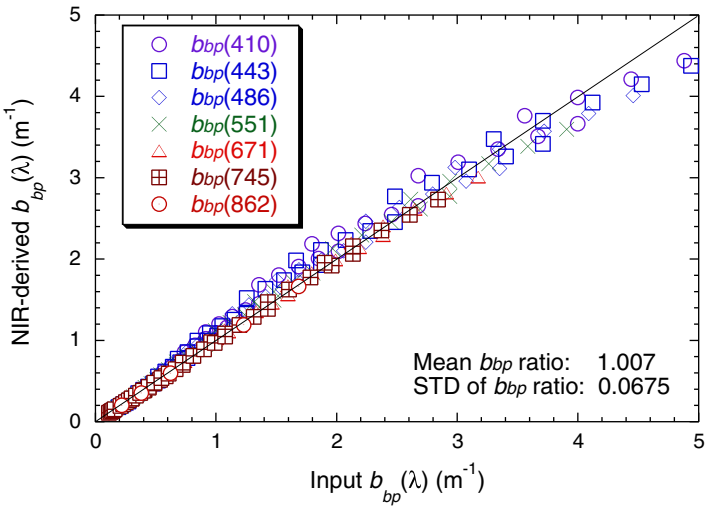

Figure 11. Scatter plot of the Hydrolight $b_{bp}(\lambda)$ input and NIR-based $b_{bp}(\lambda)$ for VIIRS spectral bands at 410, 443, 486, 551, 671, 745, and 862 nm.

Due to the unavailability of the in situ $b_{bp}(\lambda)$ data in the turbid waters, and also the high uncertainty in the in situ $b_{bp}(\lambda)$ measurements, Hydrolight simulations were used to characterize, quantify, and evaluate the NIR-based $b_{bp}(\lambda)$ algorithm in coastal turbid waters. Figure 11 shows the scatter plot of Hydrolight input $b_{bp}(\lambda)$ and the NIR-based $b_{bp}(\lambda)$ retrievals derived using $nL_w(\lambda)$ spectra from Hydrolight outputs. Average mineral type is used in the simulations with Chl-a to be 20 mg/m^3, $a_g(440)$ to be 1.0 m^{-1}, TSM ranging from 10 to 200 mg/L and $b_{bp}(\lambda)$ ratio from 0.015 to 0.025, which are typical for coastal turbid waters (Zhang et al., 2010a, 2010b).

Table 1 provides the statistics from the comparison of the Hydrolight $b_{bp}(\lambda)$ and the NIR-based $b_{bp}(\lambda)$. In general, the NIR-based $b_{bp}(\lambda)$ matches well with the Hydrolight input $b_{bp}(\lambda)$. The correlation coefficients for $b_{bp}(\lambda)$ in the VIIRS bands are over 0.99. The mean and standard deviation (STD) of $b_{bp}(\lambda)$ ratio $(b_{bp}^{(NIR)}(\lambda)/b_{bp}^{(input)}(\lambda))$ for all $b_{bp}(\lambda)$ are 1.00748 and 0.0675. The mean ratio in $b_{bp}(\lambda)$ ranges from 1.04704 for $b_{bp}(\lambda)$ at 410 nm to 0.960866 at 862 nm. On the other hand, the STD value monotonously increases from 0.027403 at 862 nm to 0.095955 at 410 nm. This is mainly attributed to the extrapolation error that mathematically extrapolates $b_{bp}(\lambda)$ from the NIR 862 to 410 nm.

The assumption $a_w(\lambda) \gg a_d(\lambda)$ in the NIR wavelengths is generally valid for turbid waters, thus equation (5) can be used in the NIR-based IOP computation. For extremely turbid waters, the approximation in equation (5) can still hold due to the fact that $b_{bp}(\lambda)$ at the NIR wavelengths is one to two orders higher than $a_d(\lambda)$ even though it is possible that $a_d(\lambda)$ is not negligible in comparison to $a_w(\lambda)$ in extremely turbid waters. Thus, the NIR-based $b_{bp}(\lambda)$ algorithm can be applied to highly turbid waters to derive reasonably accurate $b_{bp}(\lambda)$ in the NIR and visible bands.

To examine the robustness of the NIR-based $b_{bp}(\lambda)$ algorithm, we further extend the TSM to 300–500 mg/L for very extremely turbid waters. Even though these extremely turbid waters are not observed in the satellite climatology in terms of $nL_w(\lambda)$ and $b_{bp}(\lambda)$ values, they can indeed occur in nature under some ocean and atmosphere events such as a strong tropical storm, an abnormal tidal current, etc. In these simulations, $b_{bp}(\lambda)$ in the NIR wavelength can reach over 15–20 m^{-1} (results not shown). Table 2 shows comparison results between the Hydrolight $b_{bp}(\lambda)$ input and NIR-based $b_{bp}(\lambda)$ retrievals. Overall, the mean ratio is 0.9851 with the STD of 0.0394. The correlation between the input $b_{bp}(\lambda)$ and the NIR-based $b_{bp}(\lambda)$ is 0.9925. These statistics for the extremely turbid waters are similar to those for the regular turbid waters with TSM ranging between 10 and 200 mg/L. It provides further evidence that this NIR-based $b_{bp}(\lambda)$ algorithm can be safely used to derive VIIRS $b_{bp}(\lambda)$ products for global highly turbid waters.

One key procedure to retrieve $b_{bp}(\lambda)$ from satellite observations is the determination of the power law slope η. In the GSM IOP algorithm, η is set to be a generally fixed value, while η is empirically derived in the QAA and GIOP using $nL_w(\lambda)$ in the visible bands. Highly dynamic features of η (Loisel et al., 2006; Stramski et al.,

Table 1
Statistics for Particle Backscattering Ratio for Turbid Waters With TSM of 10–200 mg/L

Statistics parameters	Ratio of $b_{bp}(\lambda)$ between the NIR-derived and Hydrolight input values							
	$b_{bp}(410)$	$b_{bp}(443)$	$b_{bp}(486)$	$b_{bp}(551)$	$b_{bp}(671)$	$b_{bp}(745)$	$b_{bp}(862)$	All
Mean	1.0470	1.0378	1.0260	1.0134	0.9932	0.9740	0.9609	1.0075
Median	1.0581	1.0512	1.0339	1.0138	0.9868	0.9684	0.9587	0.9893
STD	0.0960	0.0839	0.0696	0.0535	0.0276	0.0235	0.0274	0.0675
Correlation coefficient	0.9912	0.9929	0.9949	0.9968	0.9989	0.9994	0.9997	0.9946

Table 2
Statistics for Particle Backscattering Ratio for Turbid Waters With TSM of 300–500 mg/L

Statistics parameters	Ratio of $b_{bp}(\lambda)$ between the NIR-derived and Hydrolight input values							
	$b_{bp}(410)$	$b_{bp}(443)$	$b_{bp}(486)$	$b_{bp}(551)$	$b_{bp}(671)$	$b_{bp}(745)$	$b_{bp}(862)$	All
Mean	0.9660	0.9680	0.9737	0.9845	0.9948	0.9993	1.0096	0.9851
Median	0.9559	0.9605	0.9697	0.9848	1.0012	0.9962	1.0086	0.9908
STD	0.0524	0.0477	0.0418	0.0350	0.0258	0.0231	0.0236	0.0394
Correlation coefficient	0.9882	0.9895	0.9912	0.9931	0.9955	0.9964	0.9969	0.9925

2007) and the saturation of $nL_w(\lambda)$ in the turbid coastal and inland waters determine that these $b_{bp}(\lambda)$ algorithms perform poorly in the turbid coastal waters especially highly turbid waters.

Power slope η is related to the particle size distributions (PSDs), i.e., $\zeta \approx \eta - 3$ (Babin et al., 2003; Kostadinov et al., 2009; Morel, 1973), where ζ is the power law slope of the Junge-type (Junge, 1963) size distributions (Balder, 1970; Sheldon et al., 1972; Twardowski et al., 2001). In fact, particle backscattering properties are determined by particle size distribution, particle shapes, and composition. However, particle size distribution is the dominant factor in determining the particle scattering features such as the backscattering power law slope and the backscattering ratio (Kostadinov et al., 2009; Ulloa et al., 1994). For most of the satellite-derived global $b_{bp}(\lambda)$ and the available in situ observations, particle backscattering power law slope η is typically positive or close to 0 (Loisel et al., 2006; Reynolds et al., 2016; Stramski et al., 2007; Wozniak & Stramski, 2004). This shows that $b_{bp}(\lambda)$ decreases with the wavelength for VIIRS-derived $b_{bp}(410)$ to $b_{bp}(862)$. However, η may also be negative for large size particles (Kostadinov et al., 2009). Correspondingly, $b_{bp}(\lambda)$ in the NIR wavelengths thus are larger than those in the visible bands. In China's east coastal region, in situ $b_{bp}(\lambda)$ can indeed increase with the wavelength at some highly turbid locations (Zhang et al., 2010a).

In this study, VIIRS-derived $b_{bp}(\lambda)$ images in the five turbid regions (Figures 3–7) and $b_{bp}(\lambda)$ at the eight stations (Figure 8) show that the particle size distribution in the water column is highly dynamic depending on the regions and the seasons. At Stations 1 and 2 in China's east coastal region, $b_{bp}(\lambda)$ increases with the increase of the wavelength during the winter season, while $b_{bp}(\lambda)$ decreases with the wavelength during the summer season. This shows that the η is negative in the winter and positive in the summer, and might further suggest that the particle size is bigger in the winter ($\zeta < -3$) than that in the summer ($\zeta > -3$). The seasonal variation of particle size distribution in the water column may be attributed to the seasonal variability of the turbulence and water mixing process driven by the seasonal monsoon in China's east coastal region (Shi & Wang, 2010a, 2012a).

At Station 4 in the Amazon River Estuary (Figure 8d) and Station 7 in the Meghna River Estuary (Figure 8g), $b_{bp}(\lambda)$ increases with increase of the wavelength for all seasons, while $b_{bp}(\lambda)$ decreases with the increase of the wavelength for all seasons at Station 6 in the La Plata River Estuary (Figure 8f) and Station 8 in Atchafalaya River Estuary (Figure 8h). This further suggests that the particle sizes at Stations 4 and 7 are generally larger than those at Stations 6 and 8. At Station 3 in Lake Taihu (Figure 8c) and Station 5 in the Amazon River's north branch (Figure 8e), $b_{bp}(\lambda)$ is generally flat for all seasons, implying that particle size in the water column is more or less the same even though $b_{bp}(\lambda)$ can vary seasonally at these two stations. It is also noted that $b_{bp}(\lambda)$ power law slope is still positive even though $nL_w(\lambda)$ at the NIR bands in the La Plata River Estuary is similar to that in China's east coastal region (Figure 2). This indicates that $b_{bp}(\lambda)$ power law slope is not only seasonal-dependent, but also regional-dependent. If $nL_w(\lambda)$ at the NIR bands is approximated as the surrogate of the TSM concentration, the particle size in the La Plata River Estuary is smaller than that in China's east coastal region even though the TSM concentration at these two regions is similar.

This study also has significant implications for retrieving other IOPs such as phytoplankton absorption spectra $a_{ph}(\lambda)$. With known $b_{bp}(\lambda)$ in the visible over turbid coastal and inland waters, similar procedures in the other IOP modeling approaches such as QAA and GSM can be implemented to produce $a_{ph}(\lambda)$ and $a_{dg}(\lambda)$ for global turbid coastal and inland waters. Alternatively, the NIR-based $b_{bp}(\lambda)$ can also provide the potential to further tune the regional algorithms in order to accurately derive optical and biogeochemical products such as $b_{bp}(\lambda)$, $a_{ph}(\lambda)$, Chl-a, and TSM.

5. Conclusion

In this study, we developed an NIR-based $b_{bp}(\lambda)$ algorithm for turbid coastal and inland waters. This algorithm is based on the fact that the water absorption coefficients, $a_w(\lambda)$, at the NIR wavelengths are much larger than other components like $a_{iop}(\lambda)$. The NIR-based $b_{bp}(\lambda)$ algorithm is assessed and compared with other $b_{bp}(\lambda)$ algorithms such as QAA, showing that the NIR-based algorithm produces significantly larger $b_{bp}(\lambda)$ data over highly turbid coastal and inland waters.

The advantages and disadvantages of these $b_{bp}(\lambda)$ algorithms are also addressed, and a combination of the NIR-based and QAA-based algorithms has been proposed and demonstrated. The combined $b_{bp}(\lambda)$ algorithm in China's east coastal region shows that high quality $b_{bp}(\lambda)$ can be retrieved for both the open ocean and turbid coastal and inland waters. The implications of the NIR-based $b_{bp}(\lambda)$ algorithm for deriving other ocean color products such as $a_{ph}(\lambda)$, Chl-a, TSM, etc. in the turbid coastal and inland waters are also discussed.

Using the NIR-based $b_{bp}(\lambda)$ algorithm, we have characterized and quantified $b_{bp}(\lambda)$ in the major turbid waters of the global ocean with VIIRS-SNPP observations between 2012 and 2016. Seasonal and interannual variations of $b_{bp}(\lambda)$ in China's east coastal region, the Amazon River Estuary, the La Plata River Estuary, the Meghna River Estuary, and the Atchafalaya River Estuary are analyzed. $b_{bp}(\lambda)$ can reach over $\sim$3–4 m^{-1} in some highly turbid regions. In China's east coastal region, $b_{bp}(\lambda)$ data show significant seasonal variations in the Subei Shoal, Hangzhou Bay, and inland Lake Taihu. In particular, VIIRS-derived $b_{bp}(\lambda)$ data in the winter season is remarkably higher than those in the summer season. The Amazon River Estuary is identified as the most turbid region in the global ocean in terms of the $b_{bp}(\lambda)$ magnitude. No significant seasonal variations of $b_{bp}(\lambda)$ in the Amazon River Estuary are found.

We also found that $b_{bp}(\lambda)$ spectra in these five highly turbid regions are seasonal-dependent and regional-dependent. In highly turbid waters of China's east coastal region, $b_{bp}(\lambda)$ power law slope, η, is negative in the winter season with increasing $b_{bp}(\lambda)$ from wavelength of 410 to 862 nm, and slightly negative or flat in the other seasons. In the Amazon River Estuary, power law slope, η, of $b_{bp}(\lambda)$ is mostly negative for all seasons. Flat $b_{bp}(\lambda)$ spectra are found in Lake Taihu. In the La Plata River Estuary and the Atchafalaya River Estuary, power law slopes, η, of $b_{bp}(\lambda)$ is positive for all seasons with decreasing $b_{bp}(\lambda)$ from the wavelength of 410 to 862 nm. The intrinsic relationship between $b_{bp}(\lambda)$ power law slopes and the particle size distributions in the water column implies that the particle sizes in the water column of the Amazon River Estuary and China's east coastal region are generally larger than those in the La Plata River Estuary and the Atchafalaya River Estuary.

Acknowledgments
The VIIRS ocean color data imageries and calibration/validation results can be found at the NOAA Ocean Color Team website (https://www.star.nesdis.noaa.gov/sod/mecb/color/) and VIIRS mission-long ocean color data are freely available through the NOAA CoastWatch website (https://coastwatch.noaa.gov/). We thank two anonymous reviewers for their useful comments. The views, opinions, and findings contained in this paper are those of the authors and should not be construed as an official NOAA or U.S. Government position, policy, or decision.

References

Babin, M., Morel, A., Fournier-Sicre, V., Fell, F., & Stramski, D. (2003). Light scattering properties of marine particles in coastal and open ocean waters as related to the particle mass concentration. *Limnology and Oceanography: Methods*, *48*(2), 843–859.

Bailey, S. W., Franz, B. A., & Werdell, P. J. (2010). Estimation of near-infrared water-leaving reflectance for satellite ocean color data processing. *Optics Express*, *18*, 7521–7527.

Balder, H. (1970). The hyperbolic distribution of particle sizes. *Journal of Geophysical Research*, *75*(15), 2822–2830. https://doi.org/10.1029/JC075i015p02822

Clark, D. K., Gordon, H. R., Voss, K. J., Ge, Y., Broenkow, W., & Trees, C. (1997). Validation of atmospheric correction over the ocean. *Journal of Geophysical Research*, *102*(D14), 17209–17217. https://doi.org/10.1029/96JD03345

Doron, M., Belanger, S., Doxaran, D., & Babin, M. (2011). Spectral variations in the near-infrared ocean reflectance. *Remote Sensing of Environment*, *115*(7), 1617–1631. https://doi.org/10.1016/j.rse.2011.01.015

Doxaran, D., Froidefond, J. M., Lavender, S., & Castaing, P. (2002). Spectral signature of highly turbid waters—Application with SPOT data to quantify suspended particulate matter concentrations. *Remote Sensing of Environment*, *81*(1), 149–161. https://doi.org/10.1016/S0034-4257(01)00341-8

Esaias, W. E., Abbott, M. R., Barton, I., Brown, O. B., Campbell, J. W., Carder, K. L.,. . . Minnett, P. J. (1998). An overview of MODIS capabilities for ocean science observations. *IEEE Transactions on Geoscience and Remote Sensing*, *36*(4), 1250–1265. https://doi.org/10.1109/36.701076

Garver, S. A., & Siegel, D. A. (1997). Inherent optical property inversion of ocean color spectra and its biogeochemical interpretation: 1. Time series from the Sargasso Sea. *Journal of Geophysical Research*, *102*(C8), 18607–18625. https://doi.org/10.1029/96JC03243

Gitelson, A. A., Schalles, J. F., & Hladik, C. M. (2007). Remote chlorophyll-a retrieval in turbid, productive estuaries: Chesapeake Bay case study. *Remote Sensing of Environment*, *109*, 464–472. https://doi.org/10.1016/j.rse.2007.01.016

Goldberg, M. D., Kilcoyne, H., Cikanek, H., & Mehta, A. (2013). Joint Polar Satellite System: The United States next generation civilian polar-orbiting environmental satellite system. *Journal of Geophysical Research: Atmosphere*, *118*, 13463–13475. https://doi.org/10.1002/2013JD020389

Gordon, H. R., Brown, O. B., Evans, R. H., Brown, J. W., Smith, R. C., Baker, K. S., & Clark, D. K. (1988). A semianalytic radiance model of ocean color. *Journal of Geophysical Research*, *93*(D9), 10909–10924. https://doi.org/10.1029/JD093id09p10909

Gordon, H. R., Clark, D. K., Mueller, J. L., & Hovis, W. A. (1980). Phytoplankton pigments from the Nimbus-7 Coastal Zone Color Scanner: Comparisons with surface measurements. *Science*, *210*, 63–66.
Gordon, H. R., & Morel, A. (1983). *Remote assessment of ocean color for interpretation of satellite visible imagery: A review*. New York: Springer.
Gordon, H. R., & Wang, M. (1994). Retrieval of water-leaving radiance and aerosol optical thickness over the oceans with SeaWiFS: A preliminary algorithm. *Applied Optics*, *33*, 443–452.
Hoge, F. E., & Lyon, P. E. (1996). Satellite retrieval of inherent optical properties by linear matrix inversion of oceanic radiance models: An analysis of model and radiance measurement errors. *Journal of Geophysical Research*, *101*(C7), 16631–16648. https://doi.org/10.1029/96JC01414
Hovis, W. A., Clark, D. K., Anderson, F., Austin, R. W., Wilson, W. H., Baker, E. T.,. . . Yentsch, C. S. (1980). Nimbus 7 Coastal Zone Color Scanner: System description and initial imagery. *Science*, *210*, 60–63.
Hu, C., Li, D., Chen, C., Ge, J., Muller-Karger, F. E., Liu, J.,. . . He, M. X. (2010). On the recurrent *Ulva prolifera* blooms in the Yellow Sea and East China Sea. *Journal of Geophysical Research*, *115*, C05017. https://doi.org/10.1029/2009JC005561
Huang, J., Chen, L. Q., Chen, X. L., Tian, L. Q., Feng, L., Yesou, H., & Li, F. F. (2014). Modification and validation of a quasi-analytical algorithm for inherent optical properties in the turbid waters of Poyang Lake, China. *Journal of Applied Remote Sensing*, *8*(1), 083587. https://doi.org/10.1117/1.JRS.8.083587
IOCCG (2006). Remote sensing of inherent optical properties: Fundamentals, tests of algorithms, and applications. In Z. Lee (Ed.), *Reports of the International Ocean-Colour Coordinating Group* (No. 5, p. 125). Dartmouth, Canada: IOCCG.
IOCCG (2010). Atmospheric correction for remotely-sensed ocean-colour products. In M. Wang (Ed.), *Reports of International Ocean-Color Coordinating Group* (No. 10, p. 77). Dartmouth, Canada: IOCCG.
Jiang, L. D., & Wang, M. H. (2014). Improved near-infrared ocean reflectance correction algorithm for satellite ocean color data processing. *Optics Express*, *22*(18), 21657–21678.
Junge, C. E. (1963). *Air chemistry and radioactivity*. New York, NY: Academic.
Knaeps, E., Ruddick, K. G., Doxaran, D., Dogliotti, A. I., Nechad, B., Raymaekers, D., & Sterckx, S. (2015). A SWIR based algorithm to retrieve total suspended matter in extremely turbid waters. *Remote Sensing of Environment*, *168*, 66–79.
Kostadinov, T. S., Siegel, D. A., & Maritorena, S. (2009). Retrieval of the particle size distribution from satellite ocean color observations. *Journal of Geophysical Research: Oceans*, *114*, C09015. https://doi.org/10.1029/2009JC005303
Lavender, S. J., Pinkerton, M. H., Moore, G. F., Aiken, J., & Blondeau-Patissier, D. (2005). Modification to the atmospheric correction of SeaWiFS ocean colour images over turbid waters. *Continental Shelf Research*, *25*(4), 539–555. https://doi.org/10.1016/j.csr.2004.10.007
Le, C. F., Li, Y. M., Zha, Y., Sun, D. Y., & Yin, B. (2009). Validation of a quasi-analytical algorithm for highly turbid eutrophic water of Meiliang Bay in Taihu Lake, China. *IEEE Transactions on Geoscience and Remote Sensing*, *47*(8), 2492–2500.
Lee, Z. P., Carder, K. L., & Arnone, R. A. (2002). Deriving inherent optical properties from water color: A multiband quasi-analytical algorithm for optically deep waters. *Applied Optics*, *41*(27), 5755–5772. https://doi.org/10.1364/Ao.41.005755
Loisel, H., Nicolas, J. M., Sciandra, A., Stramski, D., & Poteau, A. (2006). Spectral dependency of optical backscattering by marine particles from satellite remote sensing of the global ocean. *Journal of Geophysical Research: Oceans*, *111*, C09024. https://doi.org/10.1029/2005JC003367
Ma, R. H., Pan, D. L., Duan, H. T., & Song, Q. J. (2009). Absorption and scattering properties of water body in Taihu Lake, China: Backscattering. *International Journal of Remote Sensing*, *30*(9), 2321–2335.
McClain, C. R. (2009). A decade of satellite ocean color observations. *Annual Review of Marine Science*, *1*, 19–42. https://doi.org/10.1146/annurev.marine.010908.163650
McClain, C. R., Feldman, G. C., & Hooker, S. B. (2004). An overview of the SeaWiFS project and strategies for producing a climate research quality global ocean bio-optical time series. *Deep-Sea Research, Part II*, *51*(1–3), 5–42. https://doi.org/10.1016/j.dsr2.2003.11.001
Miller, R. L., & McKee, B. (2004). Using MODIS Terra 250 m imagery to map concentrations of total suspended matter in coastal waters. *Remote Sensing of Environment*, *93*, 259–266.
Mobley, C. D., Gentili, B., Gordon, H. R., Jin, Z. H., Kattawar, G. W., Morel, A.,. . . Stavn, R. H. (1993). Comparison of numerical-models for computing underwater light fields. *Applied Optics*, *32*(36), 7484–7504.
Morel, A. (Ed.) (1973). *Diffusion de la lumière par les eaux de mer. Résultats expérimentaux et approche théorique* (pp. 1–76). London, UK: Optics of the Sea, AGARD Lect. Ser.
Nezlin, N. P., DiGiacomo, P. M., Diehl, D. W., Jones, B. H., Johnson, S. C., Mengel, M. J.,. . . Wang, M. (2008). Stormwater plume detection by MODIS imagery in the southern California coastal ocean. *Estuarine, Coastal and Shelf Science*, *80*, 141–152.
O'Reilly, J. E., Maritorena, S., Mitchell, B. G., Siegel, D. A., Carder, K. L., Garver, S. A.,. . . McClain, C. (1998). Ocean color chlorophyll algorithms for SeaWiFS. *Journal of Geophysical Research*, *103*(C11), 24937–24953. https://doi.org/10.1029/98JC02160
Qing, S., Tang, J. W., Cui, T. W., & Zhang, J. (2011). Retrieval of inherent optical properties of the Yellow Sea and East China Sea using a quasi-analytical algorithm. *Chinese Journal of Oceanology and Limnology*, *29*(1), 33–45.
Reynolds, R. A., Stramski, D., & Neukermans, G. (2016). Optical backscattering by particles in Arctic seawater and relationships to particle mass concentration, size distribution, and bulk composition. *Limnology and Oceanography: Methods*, *61*(5), 1869–1890.
Ruddick, K. G., Ovidio, F., & Rijkeboer, M. (2000). Atmospheric correction of SeaWiFS imagery for turbid coastal and inland waters. *Applied Optics*, *39*(6), 897–912. https://doi.org/10.1364/Ao.39.000897
Sheldon, R. W., Sutcliffe, W. H., & Prakash, A. (1972). Size distribution of particles in the *ocean. Limnology and Oceanography: Methods*, *17*(3), 327–340.
Shen, F., Salama, M. S., Zhou, Y. X., Li, J. F., Su, Z. B., & Kuang, D. B. (2010b). Remote-sensing reflectance characteristics of highly turbid estuarine waters—A comparative experiment of the Yangtze River and the Yellow River. *International Journal of Remote Sensing*, *31*(10), 2639–2654.
Shen, F., Verhoef, W., Zhou, Y. X., Salama, M. S., & Liu, X. L. (2010a). Satellite estimates of wide-range suspended sediment concentrations in Changjiang (Yangtze) Estuary using MERIS data. *Estuaries Coasts*, *33*(6), 1420–1429.
Shi, W., & Wang, M. (2009a). Satellite observations of flood-driven Mississippi River plume in the spring of 2008. *Geophysical Research Letters*, *36*, L07607. https://doi.org/10.1029/2009GL037210
Shi, W., & Wang, M. (2009b). An assessment of the black ocean pixel assumption for MODIS SWIR bands. *Remote Sensing of Environment*, *113*(8), 1587–1597. https://doi.org/10.1016/j.rse.2009.03.011
Shi, W., & Wang, M. (2009c). Green macroalgae blooms in the Yellow Sea during the spring and summer of 2008. *Journal of Geophysical Research*, *114*, C12010. https://doi.org/10.1029/2009JC005513
Shi, W., & Wang, M. (2010a). Satellite observations of the seasonal sediment plume in central East China Sea. *Journal of Marine Systems*, *82*(4), 280–285. https://doi.org/10.1016/j.jmarsys.2010.06.002

Shi, W., & Wang, M. (2010b). Characterization of global ocean turbidity from Moderate Resolution Imaging Spectroradiometer ocean color observations. *Journal of Geophysical Research: Oceans*, *115*, C11022. https://doi.org/10.1029/2010JC006160

Shi, W., & Wang, M. (2012a). Satellite views of the Bohai Sea, Yellow Sea, and East China Sea. *Progress in Oceanography*, *104*, 30–45. https://doi.org/10.1016/j.pocean.2012.05.001

Shi, W., & Wang, M. (2012b). Sea ice properties in the Bohai Sea measured by MODIS-Aqua: 1. Satellite algorithm development. *Journal of Marine Systems*, *95*, 32–40. https://doi.org/10.1016/j.jmarsys.2012.01.012

Shi, W., & Wang, M. (2012c). Sea ice properties in the Bohai Sea measured by MODIS-Aqua: 2. Study of sea ice seasonal and interannual variability. *Journal of Marine Systems*, *95*, 41–49. https://doi.org/10.1016/j.jmarsys.2012.01.010

Shi, W., & Wang, M. (2014). Ocean reflectance spectra at the red, near-infrared, and shortwave infrared from highly turbid waters: A study in the Bohai Sea, Yellow Sea, and East China Sea. *Limnology and Oceanography: Methods*, *59*(2), 427–444. https://doi.org/10.4319/lo.2014.59.2.0427

Shi, W., Wang, M., & Jiang, L. (2011). Spring-neap tidal effects on satellite ocean color observations in the Bohai Sea, Yellow Sea, and East China Sea. *Journal of Geophysical Research: Oceans*, *116*, C12932. https://doi.org/10.1029/2011JC007234

Siegel, D. A., Wang, M. H., Maritorena, S., & Robinson, W. (2000). Atmospheric correction of satellite ocean color imagery: The black pixel assumption. *Applied Optics*, *39*(21), 3582–3591. https://doi.org/10.1364/AO.39.003582

Son, S., & Wang, M. (2012). Water properties in Chesapeake Bay from MODIS-Aqua measurements. *Remote Sensing of Environment*, *123*, 163–174. https://doi.org/10.1016/j.rse.2012.03.009

Son, S., Wang, M., & Shon, J. (2011). Satellite observations of optical and biological properties in the Korean dump site of the Yellow Sea. *Remote Sensing of Environment*, *115*, 562–572. https://doi.org/10.1016/j.rse.2010.10.002

Stramski, D., Babin, M., & Wozniak, S. B. (2007). Variations in the optical properties of terrigenous mineral-rich particulate matter suspended in seawater. *Limnology and Oceanography: Methods*, *52*(6), 2418–2433. https://doi.org/10.4319/lo.2007.52.6.2418

Twardowski, M. S., Boss, E., Macdonald, J. B., Pegau, W. S., Barnard, A. H., & Zaneveld, J. R. V. (2001). A model for estimating bulk refractive index from the optical backscattering ratio and the implications for understanding particle composition in case I and case II waters. *Journal of Geophysical Research*, *106*(C7), 14129–14142. https://doi.org/10.1029/2000JC000404

Ulloa, O., Sathyendranath, S., & Platt, T. (1994). Effect of the particle-size distribution on the backscattering ratio in seawater. *Applied Optics*, *33*(30), 7070–7077.

Wang, M. (1999). A sensitivity study of SeaWiFS atmospheric correction algorithm: Effects of spectral band variations. *Remote Sensing of Environment*, *67*, 348–359.

Wang, M. (2007). Remote sensing of the ocean contributions from ultraviolet to near-infrared using the shortwave infrared bands: Simulations. *Applied Optics*, *46*, 1535–1547.

Wang, M., & Franz, B. A. (2000). Comparing the ocean color measurements between MOS and SeaWiFS: A vicarious intercalibration approach for MOS. *IEEE Transactions on Geoscience and Remote Sensing*, *38*, 184–197.

Wang, M., Isaacman, A., Franz, B. A., & McClain, C. R. (2002). Ocean color optical property data derived from the Japanese Ocean Color and Temperature Scanner and the French Polarization and Directionality of the Earth's Reflectances: A comparison study. *Applied Optics*, *41*, 974–990.

Wang, M., Jiang, L., Liu, X., Son, S., Sun, J., Shi, W.,. . . Lance, V. (2016a, July 10–15). VIIRS ocean color products: A progress update. In *Proceedings of the IEEE international geoscience and remote sensing symposium (IGARSS)* (pp. 5848–5851), Beijing, China. https://doi.org/10.1109/IGARSS.2016.7730528

Wang, M., Liu, X., Tan, L., Jiang, L., Son, S., Shi, W.,. . . Voss, K. (2013b). Impacts of VIIRS SDR performance on ocean color products. *Journal of Geophysical Research: Atmosphere*, *118*, 10347–10360. https://doi.org/10.1002/jgrd.50793

Wang, M., & Shi, W. (2005). Estimation of ocean contribution at the MODIS near-infrared wavelengths along the east coast of the US: Two case studies. *Geophysical Research Letters*, *32*, L13606. https://doi.org/10.1029/2005GL022917

Wang, M., & Shi, W. (2007). The NIR-SWIR combined atmospheric correction approach for MODIS ocean color data processing. *Optics Express*, *15*, 15722–15733. doi:10.1364/oe.15.015722

Wang, M., & Shi, W. (2012). Sensor noise effects of the SWIR bands on MODIS-derived ocean color products. *IEEE Transactions on Geoscience and Remote Sensing*, *50*, 3280–3292.

Wang, M., Shi, W., & Jiang, L. (2012). Atmospheric correction using near-infrared bands for satellite ocean color data processing in the turbid western Pacific region. *Optics Express*, *20*(2), 741–753.

Wang, M., Shi, W., Jiang, L., & Voss, K. (2016b). NIR- and SWIR-based on-orbit vicarious calibrations for satellite ocean color sensors. *Optics Express*, *24*, 20437–20453.

Wang, M., Shi, W., & Tang, J. W. (2011). Water property monitoring and assessment for China's inland Lake Taihu from MODIS-Aqua measurements. *Remote Sensing of Environment*, *115*(3), 841–854. https://doi.org/10.1016/rse.2010.11.012

Wang, M., Son, S., & Harding, J. L. W. (2009a). Retrieval of diffuse attenuation coefficient in the Chesapeake Bay and turbid ocean regions for satellite ocean color applications. *Journal of Geophysical Research*, *114*, C10011. https://doi.org/10.1029/2009JC005286

Wang, M., Son, S., & Shi, W. (2009b). Evaluation of MODIS SWIR and NIR-SWIR atmospheric correction algorithm using SeaBASS data. *Remote Sensing of Environment*, *113*, 635–644. https://doi.org/10.1016/j.rse.2008.11.005

Wang, M., Son, S., Zhang, Y., & Shi, W. (2013a). Remote sensing of water optical property for China's inland Lake Taihu using the SWIR atmospheric correction with 1640 and 2130 nm bands. *IEEE Journal of Selected Topics in Applied Earth Observations and Remote Sensing*, *6*(6), 2505–2516. https://doi.org/10.1109/JSTARS.2013.2243820

Werdell, P. J., Franz, B. A., Bailey, S. W., Feldman, G. C., Boss, E., Brando, V. E.,. . . Mangin, A. (2013). Generalized ocean color inversion model for retrieving marine inherent optical properties. *Applied Optics*, *52*(10), 2019–2037.

Wozniak, S. B., & Stramski, D. (2004). Modeling the optical properties of mineral particles suspended in seawater and their influence on ocean reflectance and chlorophyll estimation from remote sensing algorithms. *Applied Optics*, *43*(17), 3489–3503. https://doi.org/10.1364/Ao.43.003489

Zeng, N. (1999). Seasonal cycle and interannual variability in the Amazon hydrologic cycle. *Journal of Geophysical Research*, *104*(D8), 9097–9106. https://doi.org/10.1029/1998JD200088

Zhang, M., Tang, J., Dong, Q., Song, Q., & Ding, J. (2010b). Retrieval of total suspended matter concentration in the Yellow and East China Seas from MODIS imagery. *Remote Sensing of Environment*, *114*, 392–403.

Zhang, M., Tang, J., Song, Q. J., & Dong, Q. (2010a). Backscattering ratio variation and its implications for studying particle composition: A case study in Yellow and East China seas. *Journal of Geophysical Research: Oceans*, *115*, C12014. https://doi.org/10.1029/2010JC006098

Zhang, Y., Liu, X., Yin, Y., Zhang, M., & Qin, B. (2012). A simple optical model to estimate diffuse attenuation coefficient of photosynthetically active radiation in an extremely turbid lake from surface reflectance. *Optics Express*, *20*, 20482–20493.